Amanda Langørgen

Magnetic Force Microscopy and Micromagnetic Simulations of Nanoscale Magnetic Structures and Modified Artificial Spin Ices

June 2020

Master's thesis

2020

Amanda Langørgen

NTNU
Norwegian University of Science and Technology
Faculty of Information Technology and Electrical Engineering
Department of Electronic Systems

Master's thesis

NTNU
Norwegian University of Science and Technology

NTNU
Norwegian University of Science and Technology

NTNU

Norwegian University of
Science and Technology

Magnetic Force Microscopy and Micromagnetic Simulations of Nanoscale Magnetic Structures and Modified Artificial Spin Ices

Amanda Langørgen

Nanotechnology
Submission date: June 2020
Supervisor: Erik Folven
Co-supervisor: Anders Strømberg
Einar Digernes

Norwegian University of Science and Technology
Department of Electronic Systems

Abstract

Artificial spin ices are magnetic metamaterials comprised of coupled nanomagnets placed on the sites of various lattices. They are interesting systems because they allow for tailoring of magnetic properties. Furthermore, they have the potential for use in novel applications, such as low-power computation. The main purpose of this thesis was to investigate the effect of modifying a square artificial spin ice by adding circular magnetic nanodisks into the lattices. Related to this, studies of magnetic rings and of the single nanomagnets that are the constituents of the artificial spin ices were performed to determine important and useful experimental parameters.

The investigations were carried out in a two-pronged fashion, both through micromagnetic simulations and through imaging of fabricated samples using magnetic force microscopy. The samples in the microscope were kept at cryogenic temperatures and subjected to varying applied fields. Fabrication of the samples was done using electron beam lithography at the NTNU NanoLab cleanroom facility.

From the study of the magnetic rings, the direction of the magnetic field in the magnetic force microscope was determined. Moreover, determining the switching field of 2100 single nanomagnets revealed a standard deviation of 1.8 mT relative to a mean of 46 mT, demonstrating how fabrication imperfections cause variation in properties of nominally identical magnets.

Simulations revealed that adding a disk of sufficiently large diameter to the square artificial spin ice array has a marked effect under the influence of magnetic fields. The disk acts as a nucleator for magnetization reversals of its neighboring magnets. The same effect was also partly seen in magnetic force microscopy images of physically realized samples subjected to magnetic fields. Additionally, images of the as-grown magnetization states of fabricated arrays displayed large areas of ground state ordering, and their states appeared not to be altered by the presence of the embedded disks. Artificial spin ices have a vast potential in the tailoring of properties, and here the ability to partly control where magnetization reversals start in the array is shown, which might be important with a view towards applications.

Sammendrag

Kunstige spinnis betegner magnetiske metamaterialer som består av koblede nanomagneter plassert i et gitter. De utgjør interessante system fordi de gir mulighet til å skreddersy magnetiske egenskaper. Videre har de et potensial i applikasjoner som energieffektiv dataanalyse. Hovedhensikten med denne oppgaven var å undersøke effekten av å modifisere en kvadratisk kunstig spinnis ved å inkludere sirkulære magnetiske nanodisker i gitteret. I forbindelse med dette ble det utført studier av magnetiske ringer, og av de enkelte nanomagnetene som utgjør byggesteinene til de kunstige spinnisene, for å bestemme viktige og nyttige eksperimentelle parametere.

Undersøkelsene ble utført både gjennom mikromagnetiske simuleringer, og gjennom avbildning av fabrikkerte prøver ved bruk av et magnetisk kraftmikroskop. Prøvene i mikroskopet ble holdt på kryogeniske temperaturer og utsatt for varierende magnetfelt. Fabrikasjon av de fysiske strukturene ble gjennomført med elektronstrålelitografi ved renromsfasilitetene til NTNU NanoLab.

Fra studiet av de magnetiske ringene ble retningen på magnetfeltet i det magnetiske kraftmikroskopet bestemt. Videre ble det koersive feltet til 2100 enkeltnanomagneter bestemt, hvilket ga et standardavvik på 1.8 mT relativt til et gjennomsnitt på 46 mT, som demonstrerer hvordan fabrikasjonsimperfeksjoner forårsaker variasjon i egenskapene til nominelt identiske magneter.

Simuleringer avdekket at å inkludere en magnetisk disk med tilstrekkelig stor diameter i de kunstig spinnis-gitterne gir en markert effekt ved påtrykning av et magnetfelt, ved at disken assisterer reversing av magnetiseringen til nabomagnetene. Den samme effekten ble også delvis sett i de magnetiske kraftmikroskopibildene av fysiske prøver med påføring av magnetiske felt. Bilder av magnetiseringstilstandene til fabrikkerte gitter, før påtrykning av felt, viste store områder med grunntilstandsording, og tilstandene deres så ikke ut til å bli endret av tilstedeværelsen av disker. Kunstige spinnis har et stort potensial når det gjelder å skreddersy egenskaper, og her vises muligheten til å delvis kontrollere hvor magnetiseringsreversering starter i gitteret, noe som kan være nyttig med tanke på anvendelse av disse systemene.

Preface

The work presented herein was conducted during the spring of 2020 at the Department of Electronic Systems (IES) and concludes five years of study at the Norwegian University of Science and Technology. The thesis is submitted in partial fulfilment of the requirements for the degree of Master of Science in Nanotechnology, with a specialization in Nanoelectronics. A 15 ECT specialization project was carried out prior to this during the fall of 2019, where the reproducible behavior of two different artificial spin ice geometries were investigated using magnetic force microscopy. Some parts of the theory on general magnetism is adapted from the specialization project report, and the part on the systems specification is partly reproduced (it is the same system in use).

Acknowledgements

I want to thank my three brilliant supervisors, who have made this last year an adventurous experience. I must thank my supervisor Erik Folven for letting me stay in his lab, for his guidance, and for our discussions. I must also thank him for being such a humorous and nice guy in general! To Einar Digerenes I am grateful for our discussions, your valuable feedback and for sharing your great competence. I must extend my gratitude to Anders Strømberg, who in addition to providing me with two exquisite samples, managed in a short amount of time this spring to make it possible to operate the microscope remotely. Additionally, I must thank him for training and helping me out in the lab, giving valuable feedback, and for having an enthusiasm for just about anything, which has been truly inspiring!

I would also like to thank my wonderful classmates and my family. Last, but certainly not least, I must thank Eivind. You are, put in the immortal words of Tina Turner, *simply the best.*

Trondheim, June 15, 2020
Amanda Langørgen

Contents

Chapter 1

Introduction

Motivation and Background

Processing information with less energy waste is one of the major challenges in today's (information) society, as an ever-increasing amount of our total energy consumption is taken up by the handling of digital information [1]. The remarkable progress within the information technologies has been driven forth by a continuous miniaturization – and a denser packing – of the key component, the transistor [2]. However, the continuous downscaling is impeded as we reach some fundamental limits, with dimensions becoming some atoms across. Additionally, the cramming of components leads to excessive heat waste. A shift towards more energy-efficient ways to perform computations and process information is thus needed. In this regard, a field of study is that of spintronics [3]. Spintronics aims at making use of the other fundamental property of electrons beyond their charge, namely their spin, as the information carrier.

A well-known (it has been known for mankind for over two millennia [4]) phenomenon arising from the spin property of electrons is that of magnetism. Utilizing magnetic materials to process information can provide low-energy alternatives and can be viewed as a part of the general shift from charge to spin. Magnetic materials are not newcomers to the stage of information technology, as magnetism has been at the heart of data *storage*, with devices such as hard disks and magnetic tapes (still in use on NTNU, and elsewhere) [5]. Magnet-based memory devices have the advantage of being what is called non-volatile, meaning that no energy is required to maintain their magnetic state (similar to how the compass is a device that does not demand recharging to point towards north). A small piece of magnetic material can be used to represent a bit, and a hard disk works by having many nanoscale magnets each holding on to a bit of information [6]. As such, arrays of non-interacting nanomagnets are already widespread in data storage [7]. To utilize magnetic materials for computation involves a transition from non-interacting to *interacting* nanomagnets. Arrays of interacting nanomagnets are the constituents of what are known as artificial spin ices.

Artificial spin ice denotes a class of magnetic metamaterials comprising thin film islands of ferromagnetic material (nanomagnets) arranged in various lattices and coupled to each other by virtue of their magnetic fields. The small size of the magnets makes them single domain, and an elongated geometry provides a bistable magnetization direction. The first structure was fabricated by Wang et al. [8] in 2006 and was a square artificial spin ice with nanomagnets positioned on the sites of a two-dimensional square lattice. Several geometries have since been realized and studied. The arrays are typically fabricated using lithography, and as such, there is great freedom in the lattice geometry, and the dimensions of the magnets situated on the lattice. The two most studied geometries are, however, the square, and what is known as the kagome artificial spin ice. The strength of the coupling between the magnets is determined by their distance, relative arrangement, and the dimensions of the individual magnets. The

artificial spin ices were originally intended to mimic natural spin ice materials, which are (some rather obscure) substances like dysprosium titanate [9] and holmium titanate [10]. It has since evolved into a research field in its own right, and the reader is referred to a comprehensive review by Skjærvø et al. [11] summarizing the current state of the field. These arrays of magnets feature a large number of states (where one state correspond to one specific configuration of the magnetization directions of the individual magnets, which gives 2^N unique states for an array comprising N magnets), coupling, and non-volatility, making them a potential candidate as a low-power alternative for computation [11–13].

One essential property, if ensembles of nanomagnets are to be used for computation, is the ability to control their behavior [14]. A global magnetic field can be applied to drive the magnetization state of the array from one to another, by switching the magnetization direction of individual magnets. What is harder to control is the route the array choses in doing so, that is, which magnets of the array reverse their magnetization first, and which follow. Due to variation in the nanopatterning from fabrication there will be some slight differences in the switching barrier for the magnets. The magnets with the lowest barrier reverse their magnetization first under the influence of a magnetic field, and this represents a random variation that is hard to control. An example of tailoring the route of reversals is presented in the paper by Mengotti et al. [15], where individual islands are modified to reduce/increase their switching field to a larger extent than the variation from fabrication. In this manner, they achieve the control of where reversals start. Because of the coupling, the initial reversal sets of an avalanche of reversals, which is pinned when reaching the magnets with a large switching field. Another demonstrated method for controlling the switching of individual magnets involve using the magnetic field from the magnetic force microscopy tip [7, 16]. The ability to control part of the switching process also enables unlocking many of the states that are not reached by other means. Solely applying a global magnetic field in a specific sequence and at specific angles has been shown to make the array reach a subset of states, but not all [14].

Objectives

The main objective of this work was to add a perturbation in the form of a circular nanodisk into a square artificial spin ice, and to study the effect and how it potentially altered the switching in the array. The disk is referred to as a disk defect, due to it being an element of a different shape and size added into the periodic structure of the square ice metamaterial. As emphasized above, the included modification needs to stand out from the ever-present variation in switching characteristics caused by fabrication. To this end, an idea of the extent of this variation is useful. Therefore, another objective was to quantify the disorder from fabrication in terms of the variation in switching field. Additionally, as there was some uncertainty tied to the direction of applied field in the microscope apparatus, determining the field direction was also an intent in this project work.

Outline

The thesis is organized as follows. Chapter 2 presents theory on the subject of magnetism and on artificial spin ice systems. In the following chapter, micromagnetic simulations and the simulation software mumax3 is introduced. Additionally, the fabrication process of electron beam lithography, and the chief experimental technique of magnetic force microscopy is described in this chapter. The experimental procedure is given in chapter 4. Chapter 5 contains the retrieved results and discussion. Finally, in chapter 6, a conclusion is given.

Note on units

Even though the literature on magnetism flourishes with different units (a prime example is the use of both Gauss and Oersted which are in fact equivalent in vacuum), this thesis will stick with the Système International d'Unités (SI) wherever units are given.

Note on the figures

All figures in this thesis have been made using the open source vector graphics editor *Inkscape*[1].

[1] https://inkscape.org/

Chapter 2

Theory

This chapter will present the theoretical framework necessary for interpreting and discussing the obtained results in this project. The first section deals with the broad subject of magnetism. Subsequently, the micromagnetic model is treated. The final section is devoted to artificial spin ices, and their constituents, nanomagnets. The theory on magnetism is for the most part based on *Magnetism and Magnetic Materials* by J. M. D. Coey [17] and *Magnetic Materials: Fundamentals and Applications* by Nicola A. Spaldin [18].

2.1 Magnetism

Magnetism is a term used to describe physical phenomena related to magnetic fields, circulating currents, and magnetic materials. Magnetic fields are created by electric currents and magnetized matter (both of which, in essence, are electric charges in motion). Electricity and magnetism are intimately connected, and the relation between them are described by the Maxwell equations.

There are primarily two different approaches used to describe magnetism, the *Ampèrian approach*, which treats magnetism from a circulating currents picture, and the *Coulombian approach*, which utilizes the concept of magnetic poles [19]. One can think of the magnetic poles, commonly known as the north and south pole, as somewhat analogous to electric charges. Similar to electric charges, equal poles repel each other, and opposite poles attract. The force between two magnetic poles also has a similar expression as the Coulomb law for electric charges. In one aspect, however, the analogy fails. Whereas one can talk about single electric charges, the magnetic poles always appear in pairs. This truth is expressed in one of the Maxwell equations,

$$\boldsymbol{\nabla} \cdot \mathbf{B} = 0, \tag{2.1}$$

which state that the magnetic field, $\mathbf{B}$ (here with unit tesla $\mathrm{T} = \mathrm{N/Am}$), is free from divergence. Consequently, there are no "sources" or "sinks" of magnetic field, rather the $\mathbf{B}$-field circulates. Therefore, the real building block of magnetism is – unlike electricity with its single electric charges – the magnetic dipole moment.

2.1.1 The Magnetic Dipole Moment

As stated above, the elementary magnetic unit is the magnetic dipole moment[1]. The two different approaches to describe magnetism provides two descriptions of the magnetic moment. In

[1]Throughout this thesis one will find the terms magnetic moment, moment, dipole, magnetic dipole and magnetic dipole moment used interchangeably, but we are at all times talking about *the magnetic dipole moment*.

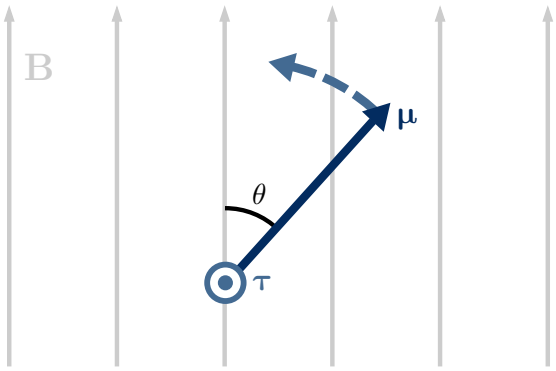

Figure 2.1: A magnetic dipole moment in a uniform magnetic field | The moment at an angle θ to a uniform **B**-field experiences a torque given by Eq. 2.2, which here points out of the paper plane. The torque acts to align the moment parallel to the field direction.

line with Ampère, the magnetic moment is equivalent to a current loop, where the value and direction of the moment is given by $\boldsymbol{\mu} = I\mathbf{A}$, where I is the current circulating in the loop, and $\mathbf{A}$ is the vector area. In the other description, the magnetic moment can be represented by two magnetic poles, $+p$ and $-p$, with a separation $\boldsymbol{\delta}$, giving a magnetic moment equal to $p\boldsymbol{\delta}$. The unit of the magnetic moment is $\mathrm{A\,m^2}$.

When a magnetic moment is placed in an external magnetic field it experiences a torque given by:

$$\boldsymbol{\tau} = \boldsymbol{\mu} \times \mathbf{B}, \tag{2.2}$$

which serves to align it with the field (Fig. 2.1), just like a magnetic compass needle rotates to align itself with earth's magnetic field[2]. If the magnetic moment arises as a consequence of some angular momentum – which it often does – then the torque on the moment will induce a precessional motion of the moment around the field axis, a phenomenon known as Larmor precession. The moment will thus not be able to fully align with the field axis unless there is a damping mechanism of the precessional motion present.

The potential energy of the magnetic dipole in the magnetic field is given by:

$$E_{\mathrm{Z}} = -\boldsymbol{\mu} \cdot \mathbf{B}. \tag{2.3}$$

This energy is often referred to as the *Zeeman energy*. The energy is defined to be zero when $\boldsymbol{\mu}$ and $\mathbf{B}$ are perpendicular and is at a minimum when $\boldsymbol{\mu}$ is parallel to $\mathbf{B}$, in which case it is negative.

If two dipoles are placed in the vicinity of one another, they will interact with each other's magnetic fields. The energy associated with this interaction can be expressed in the following equation [20]:

$$E_{\mathrm{dip}} = -\frac{\mu_0}{4\pi r^3}\left[3(\boldsymbol{\mu}_1 \cdot \hat{\mathbf{r}})(\boldsymbol{\mu}_2 \cdot \hat{\mathbf{r}}) - \boldsymbol{\mu}_1 \cdot \boldsymbol{\mu}_2\right], \tag{2.4}$$

with $\hat{\mathbf{r}} = \mathbf{r}/|\mathbf{r}|$, and $\mathbf{r}$ being the vector separating the two dipoles $\boldsymbol{\mu}_1$ and $\boldsymbol{\mu}_2$. The constant μ_0 is the permeability of vacuum and has the value $4\pi \times 10^{-7}\,\mathrm{N/A^2}$. The equation tells us that the strength of the interaction depends both on the magnitude of the dipoles, and the distance and relative orientation between them. E_{dip} favors head-to-tail (north to south) arrangements of the two dipoles.

[2] In 1600, William Gilbert published the scientific work *De Magnete*, in which he correctly suggested that the earth itself was in fact a giant magnet.

We will now turn to look at arguably the most important physical realization of a magnetic moment, the one attributed to electrons.

The Magnetic Moment of Electrons and Atoms

Electrons have an associated magnetic dipole moment. There are two contributions to this moment: orbital angular momentum related to the motion around the nucleus, and spin. To understand the relation between the orbital angular momentum and a magnetic moment we can invoke the concept of charges in motion. The electron whizzing around the nucleus can be thought of as a current loop, which we have seen generates a magnetic moment. The magnetic moment associated with the orbital angular momentum of the electron, $\mathbf{l}$, is $\boldsymbol{\mu}_\mathbf{l} = -e\mathbf{l}/2m_\mathrm{e} = \gamma\mathbf{l}$. The proportionality constant, γ, is known as the gyromagnetic ratio, and e and m_e is the electron charge and the electron mass, respectively. Different from the moment of a classical current loop, however, is that $\boldsymbol{\mu}_\mathbf{l}$ can only take on a few distinct values and orientations relative to an external field, because the orbital angular momentum of the electron is discretized. The spin of the electron, $\mathbf{s}$, is an intrinsic angular moment predicted by relativistic quantum mechanics, from which a magnetic moment of $\boldsymbol{\mu}_\mathbf{s} = \gamma\mathbf{s}$ arises, where $\gamma = -g_\mathrm{e}e/2m_\mathrm{e}$ and g_e is the electron g-factor. The spin can only take on two directions relative to a field, up or down.

An atom typically consists both of several electrons and a nucleus, and it will hold a total magnetic moment resulting from the sum of its different contributions. The spin property is not exclusive for the electrons, protons and neutrons also possess spin. However, the magnetic moment associated with the spin is as shown above inversely proportional to the particle mass, making the nuclear spin magnetic moments several orders of magnitude smaller than that associated with the electron spin. The magnetic moment of the nuclei is thus often neglected, and the total magnetic moment of an atom is attributed to its electrons[3].

The magnetic moments of the electrons add up in a manner governed by quantum mechanics. Within electron shells they tend to cancel each other out to minimize their energy, the spins arrange up and down, and the electrons whizz around the nucleus in different directions. Consequently, full electron shells have net zero orbital angular moment and net zero spin, and the existence of finite atomic magnetic moments are associated with atoms with partially filled shells [21]. The magnetic properties of atoms depend heavily on the electronic configuration, and thus, across the periodic table the magnetic properties vary.

2.1.2 Magnetization, Magnetic Fields, and Susceptibility

Knowing that atoms can possess a magnetic moment, and that materials are composed of atoms, we can continue by stating that within matter there lives a population of intrinsic magnetic dipole moments – the atomic magnetic moments. The magnetization of a material, $\mathbf{M}$, is the volume average of these intrinsic moments:

$$\mathbf{M} = \frac{\sum_V \boldsymbol{\mu}}{V}, \tag{2.5}$$

and is an important material property. The magnetization describes to which extent and in which direction the intrinsic moments are aligned.

When discussing magnetization and magnetic materials it is convenient to introduce the auxiliary magnetic field, the $\mathbf{H}$-field. As previously stated, sources of the $\mathbf{B}$-field are electric currents and magnetized matter. The circulation (the curl) of the $\mathbf{B}$-field are given by the sum of these

[3]The magnetic moment associated with the protons is however an important property utilized in the technology of magnetic resonance imaging, MRI.

contributions, expressed in Ampère's law, one of the Maxwell equations. The electric currents are commonly referred to as free currents, and can for instance be current running in a wire, as opposed to then a *bound* current in the magnetized matter. The *circulation* of the **H**-field, on the other hand, only arises from free currents. The relation between the two fields, and the magnetization, is:

$$\mathbf{B} = \mu_0(\mathbf{H} + \mathbf{M}). \tag{2.6}$$

In free space, where the magnetization, **M**, is zero, the two fields, **B** and **H**, only differ by a constant, and the conversion between them is trivial. Within a magnetized sample, the story is different. In the absence of any free currents, but in the presence of a magnetized sample, we still have an **H**-field, but the field must be conservative, $\boldsymbol{\nabla} \times \mathbf{H} = 0$. Because the **H**-field is in the direction of the **B**-field outside the material ($\mathbf{H} = \mathbf{B}/\mu_0$), the field must be in the *opposite* direction to **B**, and so to **M**, inside the material to be conservative. The **H**-field within a sample is often referred to as the demagnetizing field, while the **H**-field outside the sample (produced by the sample) is called the stray field.

The response of a material to an external field is usually expressed as **M** or **B** in response to **H**, which is chosen as the independent variable. The *susceptibility*, χ, of a material is the ratio of the magnetization to an applied field,

$$\mathbf{M} = \chi\mathbf{H}. \tag{2.7}$$

Different classes of magnetic materials can be classified based on their susceptibility.

2.1.3 Magnetic Materials

Diamagnets and Paramagnets

Most materials can be classified as being either diamagnets or paramagnets [22]. Their magnetization changes linearly in response to an external field, as shown in Fig. 2.2, and the susceptibility can therefore be considered a constant (this holds true for sufficiently small fields, as the magnetization eventually will saturate).

Diamagnetism is the weakest magnetic effect, and diamagnets are characterized by a negative and small susceptibility. When a diamagnet is placed in a magnetic field, it will gain a small magnetization in the opposite direction to the field. The diamagnetic effect is a consequence of a change in orbital motion of the electrons under the influence of an external field [23]. This response to an external field is present to some extent in all elements, but it is a small effect and only noticeable in the absence of other responses to an applied field. The materials characterized as diamagnets are those who only display the diamagnetic effect, and this is the case if there is no magnetic moment associated with the atoms in the absence of a magnetic field. All the noble gases are therefore diamagnetic, as they have filled electron shells [18].

Paramagnets are characterized by a positive and small susceptibility, however, with a larger absolute value compared to the diamagnetic susceptibility. The atoms of the paramagnets have associated finite magnetic moments, but in the absence of an external magnetic field they are disordered by thermal energy, and there is no net magnetization of the material. When a magnetic field is applied the moments tend to align with the field to lower their energy (Eq. 2.3) and thereby create a magnetization in the direction of the applied field. Once the field is removed the moments become disordered again, and the magnetization is lost. A substantial part of the elements in the periodic table are classified as paramagnets. Ferromagnets heated above their ordering temperature, called the Curie temperature (T_C), become paramagnetic.

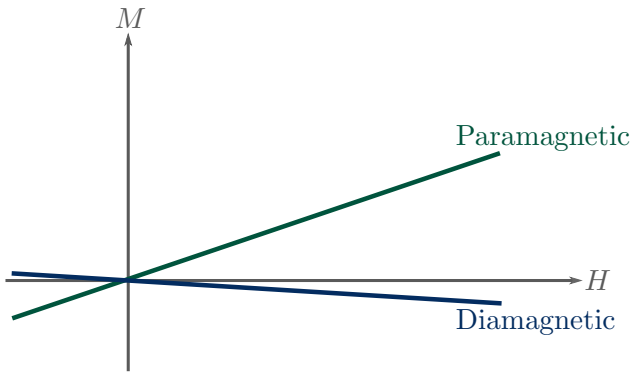

Figure 2.2: Diamagnetic and paramagnetic response to an applied field | The slope of the curves represents the susceptibility, χ. The diamagnetic curve has a negative slope, which is lower in absolute value than that of the paramagnetic response curve.

Ferromagnetism, Antiferromagnetism, and the Exchange Interaction

The response of a ferromagnet to an applied field (Fig. 2.3) is entirely different from that of the dia- and paramagnets. The intrinsic dipoles seemingly take on a life of their own and cannot be described by a linear function of the applied field, let alone a single valued one. Starting out with zero magnetization (at the origin) and applying a magnetic field one eventually reaches a saturation magnetization, M_s. Upon reducing the applied field again, the magnetization does not disappear, there is some remanent magnetization, M_r. The existence of a magnetization in the absence of magnetic fields is what gives us the permanent magnets that stick to our refrigerator doors. To return to zero magnetization, a field of a certain strength needs to be applied in the opposite direction, the coercive field H_c. The resulting relation between magnetization

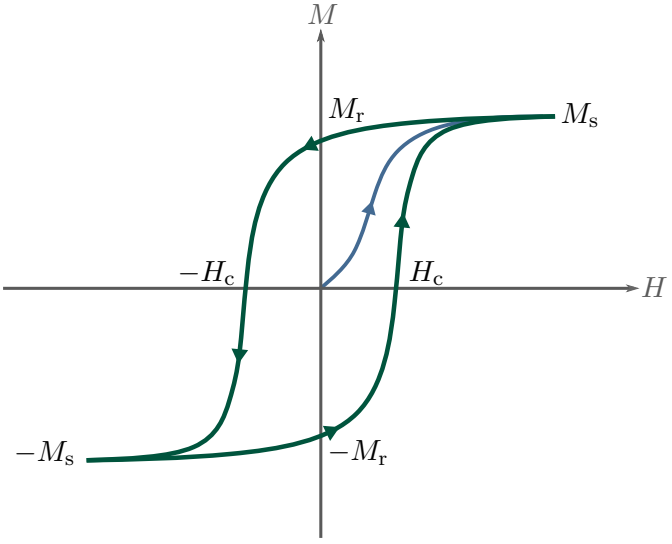

Figure 2.3: A typical hysteresis curve for a ferromagnetic material | The blue line is called the initial magnetization curve and represents the starting point where both the magnetization and the applied field is zero. At a sufficiently large applied magnetic field, the magnetization saturates at a value M_s. When the field is removed there will be some remanent magnetization M_r, and a certain field in the opposite direction, $-H_c$, must be applied to remove the magnetization. The same behavior is repeated for opposite fields tracing out a hysteresis curve.

and applied field is called a *hysteresis* loop. The three most common ferromagnetic materials are iron, cobalt, and nickel. To understand the non-linear hysteresis behavior and the existence of a permanent magnetization we need to dig a bit deeper into the structure of ferromagnetic materials.

The net magnetization retained by a ferromagnet also when there are no externally applied fields is a consequence of the magnetic moments within the ferromagnets lining up parallel to each other. Knowing that magnetic dipoles interact, one could imagine the dipolar coupling (Eq. 2.4) being the mechanism aligning the dipoles. However, the dipolar interaction is defeated by thermal energy that tends to disorder the moments for temperatures all the way down to 1 K [22] and is accordingly not the explanation for the spontaneous ordering that occurs. Indeed, the most famous ferromagnetic material – and the namesake of ferromagnetism – iron, has ordered moments up to 1000 K [21]. A stronger interaction is thus needed to explain the alignment. This stronger interaction is known as the *exchange interaction*. The exchange interaction is a quantum mechanical effect which acts between the electron spins of neighboring atoms. In ferromagnets the exchange energy is minimized by having the neighboring electron spins parallel. The existence of an exchange interaction explains why in ferromagnets, a magnetization can exist in the absence of an applied field. However, the entire hysteresis loop is not explained by this interaction, for instance why we start out with zero magnetization, or why the magnetization decreases when the field is removed if all the spins prefer to be parallel. To account for these traits, we need to introduce the concept of magnetic domains (Section 2.1.4).

There are other classes of materials where the intrinsic magnetic moments order as well. Antiferromagnetic materials are a class of materials where the exchange interaction favors anti-parallel ordering of the spin axes of neighboring atoms. The anti-parallel ordering leads to a zero net magnetization, and very different properties from the ferromagnets. The temperature above which the antiferromagnetic ordering collapses is called the Néel temperature, T_N. Fig. 2.4 summarizes how the intrinsic dipoles behave in the different classes of magnetic materials that have been mentioned.

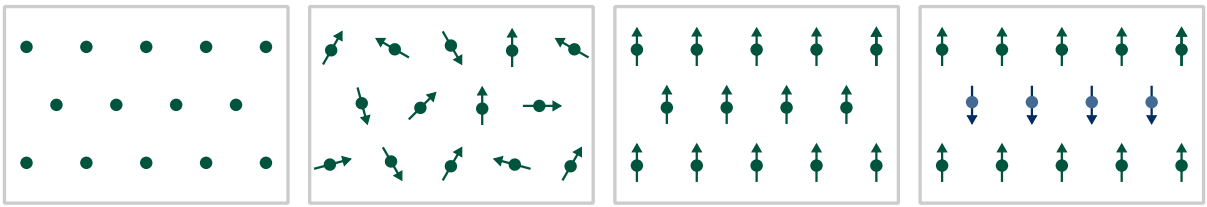

Figure 2.4: Ordering of magnetic dipole moments in magnetic materials in the absence of applied fields | **(a)** Diamagnets have no atomic magnetic moments in the absence of magnetic fields. **(b)** Paramagnetic materials have finite atomic magnetic moments that are randomly oriented. **(c)** Below T_C the moments in ferromagnets are aligned parallel. **(d)** The moments in antiferromagnets are aligned antiparallel below T_N.

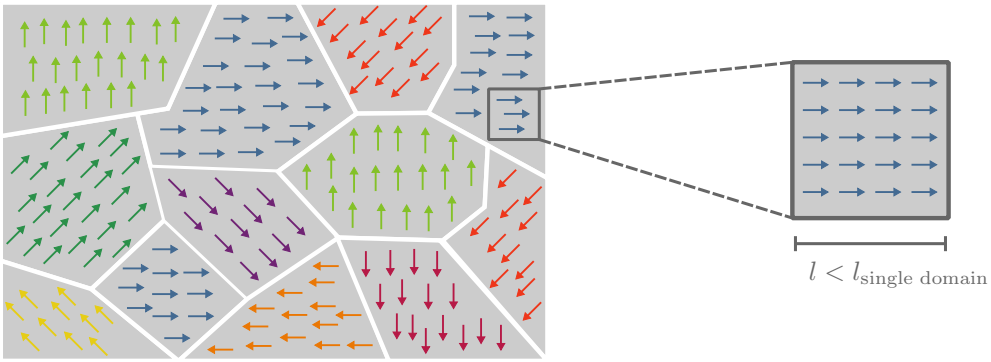

Figure 2.5: Ferromagnetic domains and the existence of a single domain limit | Left: an illustration of magnetic domains with a distribution of sizes and magnetization directions. **Right:** an illustration of a magnetic sample with sufficiently small dimensions to adopt a single domain state.

2.1.4 Domains

Despite the *ability* to retain a magnetization, a piece of ferromagnetic material will not necessarily do so. Indeed, the magnetization at the start of the blue curve in Fig. 2.3, before the magnet has been exposed to a magnetic field, is zero. The explanation lies in the existence of magnetic domains. A magnetic domain is a volume of the material where the atoms have their moments parallel. A ferromagnetic body will contain several domains, and the magnetization direction and size of the different domains will vary (Fig. 2.5). The net magnetization of an object can thus amount to zero as the different domain contributions cancel each other out.

Magnetic domains form to minimize the magnetostatic energy of a magnetic body. A piece of magnetized material creates a magnetic field, and upholding a large stray field is energy costly. Formation of domains reduces the stray field (Fig. 2.6). The formation of domains does, on the other hand, come with an energy cost associated with the exchange interaction. The different domains are separated by domain walls, which is a finite width over which the intrinsic magnetic moments reorient. Accordingly, the exchange interaction locally increases within the domain walls. One can thus talk about a domain wall energy. In addition to the exchange energy, magnetocrystalline shape anisotropy energy (Section 2.1.5) can give a contribute to the domain wall energy, as the intrinsic moments might have to deviate from low energy directions. A trade-off between the different energies involved gives the resulting domain structure.

The existence of domains is important in describing the appearance of the hysteresis curve (Fig. 2.3). In response to an increasing external field, the domains with their magnetization in a favorable direction compared to the external field first starts to grow at the expense of the other domains, through domain wall motion. When the domain walls encounter imperfections in the material, like defects, additional energy is required to move past it. When there is only one domain left in the sample, the moments reorient to align fully with the external field. Upon removal of the field the moments may reorient back, but the movement of the domain walls is not entirely reversible, because of the energy barriers created by the imperfections in the material. Therefore, after being subjected to a magnetic field, there will be some remanent magnetization in the direction of the field. With which persistence the magnet holds on to remanent magnetization when a field in the opposite direction is applied is given by the distinction between soft and hard magnets. The soft magnets are easily demagnetized, and so has a low coercive field, while the hard magnets tend to stay magnetized, and has a high coercive field.

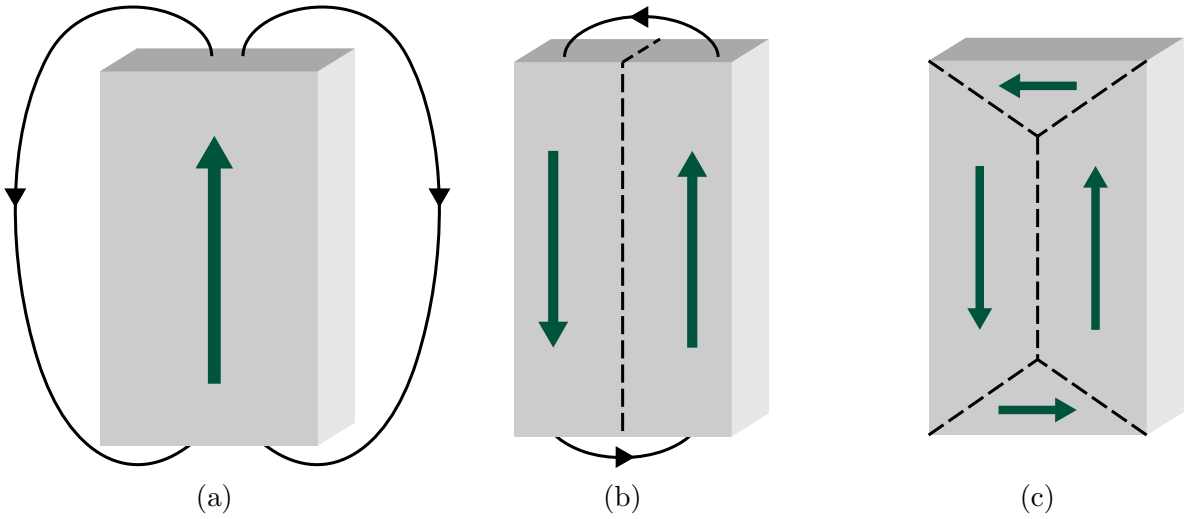

Figure 2.6: Schematic illustrations of different domain configurations with their associated stray field | The stray field, and hence the magnetostatic energy, is reduced by forming domains. **(a)** A magnet with a single domain and a large associated stray field. **(b)** Formation of two domains reduces the stray field of the magnet. **(c)** A domain configuration resulting in virtually no associated stray field, which can be referred to as a flux closure arrangement of the domains.

Single Domain Magnets

When a magnetic body is reduced below a certain size, domains do not form, because the smallness of the body makes domain wall formation energetically unfavorable. For a single domain magnet, the domain wall energy exceeds the magnetostatic energy associated with the stray field, and the magnet rather keeps the stray field than create a wall. Calculating the exact size at which a single domain state is favored over a multidomain one is not trivial [24]. A crude estimate could be to determine the width of a domain wall (which has a typical size of around 100 nm), because any particle below this size would not fit a domain wall within. For the standard ferromagnetic metals (Fe, Co, and Ni) the critical size is within some few 100 nm range [25]. The single domain magnets have their intrinsic moments aligned and are homogeneously magnetized throughout their volume (Fig. 2.5).

2.1.5 Anisotropy

Anisotropy refers to a direction dependence for the magnetization, or in other words, if there is some anisotropy present, the direction of which an external field is applied matters. Two sources of anisotropy to a magnetic sample is the magnetocrystalline anisotropy and shape anisotropy.

Magnetocrystalline anisotropy

Magnetocrystalline anisotropy is an intrinsic property of a material that causes the magnetization to prefer alignment with certain crystallographic directions. The preferred directions are termed the easy axes. As an example, in bcc Fe these are the $\langle 100 \rangle$ directions, while in Ni $\langle 111 \rangle$ are the easy axes [18]. The magnetocrystalline anisotropy energy refers to the energy required to switch the magnetization away from an easy direction. A sample will reach the same saturation magnetization in all directions, but the strength of the applied field needed to reach saturation differs.

Shape anisotropy

Magnets have the peculiar property that their magnetization depends on the shape of the magnet. For a perfectly spherical *polycrystalline* magnet there are no preferred directions of the magnetization, but whenever a magnetic sample has a larger extension in one direction, the magnetization will prefer to align along the long axis. This effect is referred to as shape anisotropy. The origin of shape anisotropy can be explained in terms of the demagnetizing field. The demagnetizing field is larger if the magnetization points along a short axis, compared to a long axis, and a larger demagnetizing field corresponds to a higher magnetostatic energy. The difference in energy between a magnetization along the long or short axis increases with an increased aspect ratio of the sample. The effect of shape anisotropy is most notable in single domain samples, in larger samples the creation of domains interferes [26].

2.2 The Micromagnetic Model

We have until now appreciated how different effects at varying length scales are at play in a ferromagnetic material. Whereas the exchange interaction has an effective range on the order of a unit cell, the magnetostatic energy is obtained by summing the contribution from every magnetic moment in the entire sample volume. *Micromagnetism* serves as a bridging theoretical framework for the study of ferromagnetic matter at intermediate length scales. Intermediate is in this context meant to denote length scales larger than the scale of atoms and single unit cells, however small enough to resolve features like magnetic domain walls. Micromagnetism is a continuum theory, where the discrete atomic structure of matter is averaged away. The magnetization is described by a continuous vector field, $\mathbf{M}(\mathbf{r}, t)$, in space, $\mathbf{r}$, and time, t. $\mathbf{M}(\mathbf{r}, t)$ has a constant magnitude equal to the saturation magnetization, M_S, and a smoothly varying direction,

$$\mathbf{M}(\mathbf{r}, t) = M_\mathrm{S}\mathbf{m}(\mathbf{r}, t), \tag{2.8}$$

where $\mathbf{m}$ is called the reduced magnetization and has unit length.

2.2.1 Micromagnetic Energy Terms

The magnetization and domain structure of a ferromagnet is a result of minimization of the total free energy, which is a sum of different contributions. The four most influential contributions are given in the equation below,

$$E_\mathrm{tot} = E_\mathrm{Z} + E_\mathrm{exch} + E_\mathrm{demag} + E_\mathrm{anis}, \tag{2.9}$$

where E_Z is the Zeeman energy, E_exch is the exchange energy, E_demag is the magnetostatic energy and E_anis is the energy attributed to magnetocrystalline anisotropy. Micromagnetism provides formulations of the different energy terms with the assumption of a continuous media.

A magnet placed in an external field has a potential energy, that is, the Zeeman energy, with a magnitude that depends on the relative orientation of its magnetization to the direction of the field. The energy of the magnetic body is given by:

$$E_\mathrm{Z} = -\int \mu_0 \mathbf{M} \cdot \mathbf{H} \mathrm{d}^3 r, \tag{2.10}$$

where $\mathbf{M} = \mathbf{M}(\mathbf{r}, t)$ is the local magnetization, and $\mathbf{H}$ is the applied field. We can recognize this expression as similar to the one given in Eq. 2.3, which was the potential energy of a single magnetic moment in an external field. For a magnetized body, the expression is cast in $\mathbf{H}$ instead of $\mathbf{B}$ and as a volume integral (over the magnetic volume) to account for the potential

energy of every moment within the body. E_{Z} is minimized if the magnetization is completely aligned with the applied field, similar to a magnetic dipole as discussed in Section 2.1.1.

The exchange energy can, in the continuum picture, be approximated by the following expression,

$$E_{\mathrm{exch}} = \int A(\boldsymbol{\nabla}\mathbf{m})^2 \mathrm{d}^3 r, \tag{2.11}$$

where A is a physical parameter of the material known as the *exchange stiffness constant*. From the equation we see that the gradient punishes varying directions of $\mathbf{m}$, since the energy increases with an increasing gradient. To minimize E_{exch} the direction of $\mathbf{m}$ should be constant everywhere ($\boldsymbol{\nabla}\mathbf{m} = 0$), which is the case if all the atomic magnetic moments are aligned. From our previous discussion on the exchange interaction, we expect this to be the lowest energy configuration in terms of exchange for a ferromagnet.

The magnetostatic self-energy is the energy associated with maintaining a stray field. It can be expressed in a similar manner as the energy caused by an external field (except for the factor 1/2)

$$E_{\mathrm{demag}} = -\frac{1}{2}\int \mu_0 \mathbf{H}_{\mathrm{d}} \cdot \mathbf{M} \mathrm{d}^3 r. \tag{2.12}$$

Here $\mathbf{H}_{\mathrm{d}}$ is the demagnetizing field. Minimization of this energy is achieved by reducing $\mathbf{H}_{\mathrm{d}}$ to a minimum, a feat that can be accomplished through the formation of domains. The demagnetizing field is, as previously stated, directed opposite to the magnetization, and E_{demag} is thus always positive (or zero). The effect of shape anisotropy (Section 2.1.5) is incorporated into this term, as the demagnetizing field depends on the shape of the sample.

A magnetocrystalline anisotropy energy term, E_{anis}, can also be expressed as a function of the local magnetization. The specific cast of the equation depends on the symmetry of the anisotropy.

A characteristic length that arises as a consequence of the competition between the exchange energy and the magnetostatic energy is the exchange length, l_{exch},

$$l_{\mathrm{exch}} = \sqrt{\frac{2A}{\mu_0 M_{\mathrm{S}}^2}}. \tag{2.13}$$

The exchange length can be thought of as a minimum length over which the direction of the magnetization can vary, or alternatively, the maximum length over which the magnetization can be considered uniform. l_{exch} is typically a few nanometers [17].

2.2.2 The Landau-Lifshitz-Gilbert Equation

If we are interested in the dynamics of a system, for instance if a time varying field is present, we need an equation involving time. Such an equation, describing the dynamics of a ferromagnetic material, is the Landau-Lifshitz Gilbert (LLG) equation [27],

$$\frac{\partial \mathbf{m}}{\partial t} = -\gamma \mathbf{m} \times \mathbf{H}_{\mathrm{eff}} + \alpha \mathbf{m} \times \frac{\partial \mathbf{m}}{\partial t}. \tag{2.14}$$

Here γ is the gyromagnetic ratio, and α is a dimensionless damping parameter. H_{eff} is an effective field, composed of the external field, as well as contributions from exchange, magnetostatic (demagnetizing) and anisotropy energy[4]. The first term on the right-hand side describes a precessional motion of the magnetization, where the axis of precession is defined by the direction

[4]The equations presented in the preceding section for the different energies, can be rewritten into equations of magnetic fields.

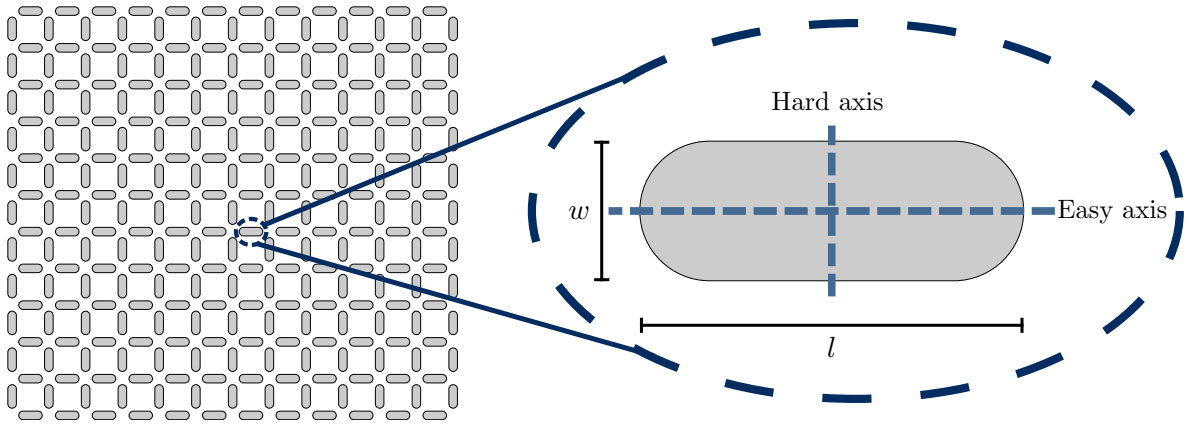

Figure 2.7: Square artificial spin ice and its building block | The artificial spin ice comprises elongated magnets, here with a stadium shape, arranged in a square lattice. The long axis of the magnet is the easy axis for the magnetization, while the short axis is the hard.

of the effective field. The second term is a phenomenological damping term, which ensures that the direction of the magnetization after some time will be aligned to the direction of the effective field, by spiraling in towards it. In solving the differential equation, one normally must resort to numerical simulations. Micromagnetic simulations and the software mumax3 will be treated in Section 3.1.

2.3 Nanomagnets and Artificial Spin Ice

Artificial spin ice denotes a magnetic metamaterial comprising (typically) elongated magnets of submicrometer dimensions (nanomagnets) positioned on a lattice (Fig. 2.7). The spatial arrangement of the magnets – the geometry – is completely governed by the experimentalist, and the magnetization of each magnet can be resolved using different microscopy techniques. Before continuing on the topic of artificial spin ice, we will, however, first direct our attention to its building blocks – tiny magnets.

2.3.1 A Tale of a Tiny Magnet

The typical dimensions of an artificial spin ice magnet are sufficiently small to make it assume a single domain state, as introduced in Section 2.1.4. Because single domain magnets have a coherent magnetization, it is possible to treat one magnet as a single magnetic dipole moment. The magnetic moment is in the direction of the magnetization, and has a value given by $m = M_S V$, where M_S is the saturation magnetization, and V is the volume of the magnet [11].

The thin and elongated geometry of the nanomagnet leads to preferred directions of the magnetic moment, dictated by shape anisotropy. The small thickness restricts the moment of the magnet to be in-plane. The elongation provides a uniaxial shape anisotropy, yielding a bistable moment (the moment prefers to point in either of the two directions along the long axis). The anisotropy energy in the case of uniaxial shape anisotropy can be represented by the following equation:

$$E_a/V = K \sin^2 \theta, \tag{2.15}$$

when the magnetization is at an angle θ to the easy axis. K is an anisotropy constant, with a value that increases with increased aspect ratio between the long and short axis (the ratio of l to w marked on Fig. 2.7.). The anisotropy energy barrier is shown in Fig. 2.8a. E_a is zero when the moment of the magnet is at angles $\theta = 0$ or $\theta = \pi$, which corresponds to alignment

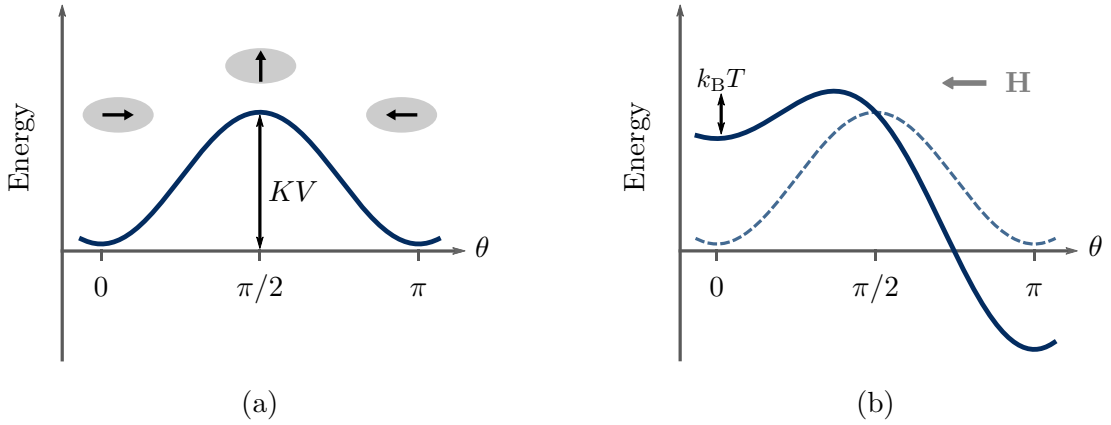

Figure 2.8: Schematics of energy landscapes for a magnet with a uniaxial shape anisotropy | **(a)** The shape anisotropy creates a barrier for magnetization reversal, equal to the anisotropy constant, K, times the volume of the magnet, V. The two energy minima correspond to the magnetization being aligned with the long axis, as illustrated with the elongated magnet and the direction of magnetization. **(b)** Application of a magnetic field will raise one side of the energy barrier by an amount equal to the Zeeman energy. If the remaining net energy barrier that must be surmounted becomes comparable to the thermal energy, the magnet might be able to reverse its magnetization.

with the long and easy axis, and at a maximum when the magnetization points along the short and hard axis of the magnet, $\theta = \pi/2$.

To switch the moment (reversal of the magnetization) from one stable direction to the opposite, energy needs to be given to the system, and applying a magnetic field can provide the energy required. The simplest model for magnetization reversal in single domain magnets is the Stoner-Wohlfarth model, where the basic premise is that the magnetization rotates coherently. Coherent rotation involves the magnetization staying uniform throughout a change of orientation. This manner of switching makes the anisotropy barrier the energy barrier that must be surmounted for a reversal to take place, because the entire magnetization must rotate through the hard direction. The switching field is thus the field that induces a Zeeman energy comparable to the anisotropy barrier. The alteration of the energy landscape for the single elongated magnet by the presence of an external field is illustrated in Fig. 2.8b. Switching occurs when one side of the barrier is raised to the point where only one minimum remains in the energy landscape. The value of the applied field necessary to switch the moment depends on the angle at which it is applied.

The single domain magnets will exhibit hysteresis despite a different manner of magnetization reversal than bulk magnetic samples. Returning to the hysteresis curve of Fig. 2.3, the rationale for its appearance was that the change in magnetization as a response to an external field was achieved through domain wall motion and the walls interacting with defects in the material as they moved. However, despite a different mechanism for magnetization reversal, a single domain nanomagnet with a defined easy axis will still have a hysteric response[5] to an applied field, as long as the field is not applied perfectly parallel to the hard axis. The hysteresis curve is a result of the existence of more than one stable magnetization state. The appearance of the curve depends on the angle at which the field is applied. For a field applied parallel to the easy axis, the hysteresis curve is square, as a consequence of two stable magnetization states of equal magnitude and opposite direction and a well-defined coercive field needed to switch between

[5]Not to be confused with a hysterical response.

them (the field necessary to overcome the anisotropy energy barrier).

The model of a coherent magnetization reversal, and a coercive field that solely depends on the anisotropy energy is challenged by the ragged nature of the real world. Real materials are inhomogenous and contain defects. Surface roughness can have an influence on the coercive field. Inhomogeneities on a sample surface may act as nucleation spots for magnetization reversal as the applied magnetic field is enhanced in their vicinity, which effectively reduces the coercive field.

The Néel-Brown Law

So far, we have left the discussion of temperature out, but temperature brings with it thermal energy which also needs to be taken into account. Thermal excitation of the magnetic moment over an energy barrier can be described by the Néel-Brown Law [28]:

$$\tau = \tau_0 \, \mathrm{e}^{\frac{\Delta E}{k_\mathrm{B} T}}, \tag{2.16}$$

where τ is a relaxation time, and τ_0 is the inverse of an attempt frequency, typically on the order of 10^{-10} to 10^{-11} s. What is evident from the equation above is that when the energy barrier is reduced to the point where it becomes comparable to thermal energy ($k_\mathrm{B}T$), the switching of the magnetization happens in a spontaneous manner, a phenomenon known as superparamagnetism. The barrier can be lowered by decreasing the volume of the magnet, and superparamagnetism is a form of magnetism attributed to very small magnetic particles. The nanomagnets of the artificial spin ice often (but not always [12]), however, have an energy barrier which is substantially larger than the thermal energy (within reasonable temperatures), leading to long mean times and what can be considered frozen moments. Thermal energy can, nonetheless, act as a small addition to an applied magnetic field (Fig. 2.8b).

2.3.2 Artificial Spin Ice

The artificial spin ices are ensembles of magnets of the kind discussed in the preceding section. The magnets are islands of thin film ferromagnetic materials such as permalloy (which is an alloy with a composition close to $Ni_{80}Fe_{20}$, possessing effectively zero magnetocrystalline anisotropy [8]) fabricated by lithography processes (Section 3.2). With their single domain state, and two stable orientations of their magnetization, they can be treated as single magnetic moments that can point in one of two directions. The moment is therefore often referred to as a macrospin [11]. Analogous to the spins of naturally occurring magnetic materials, like ferro- and antiferromagnets, the macrospins of the artificial spin ices interact. However, unlike its natural counterparts, the coupling is indeed the dipolar interaction (Eq. 2.4). The coupling of the magnets is what makes the artificial spin ice a magnetic *metamaterial*, because it gains properties beyond its constituents.

One important property that arises from the coupling is that of frustration, which can be defined as an inability to satisfy all interactions at the same time [14]. To understand the origin of frustration we can look at the archetypal square ice and the vertices where four magnets meet, see Fig. 2.9a. There are 16 different ways to arrange the moments in a vertex, but no arrangement manages to simultaneously minimize the interactions between the magnets. It is common to classify the vertex types based on their energy from the dipolar couplings. The type I arrangement has the lowest energy, followed by type II, and then type III. The type IV arrangement where all moments point in or all moments point out is the least favorable and highest energy configuration. None of the vertex configurations manages to minimize all the

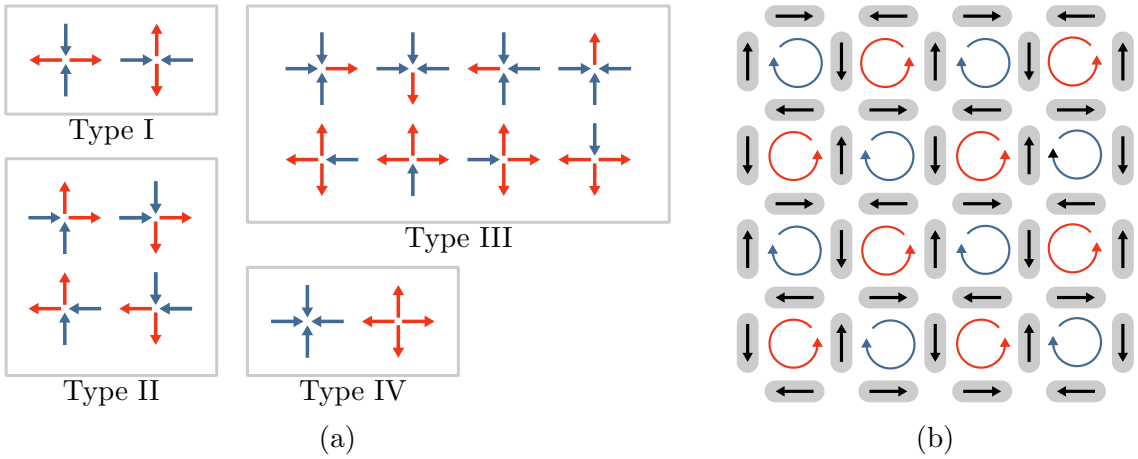

Figure 2.9: The different vertex types of the square artificial spin ice and the ground state ordering | **(a)** The 16 different ways to arrange the moments of the square ice classified by their energy from the dipolar couplings. Type I with a symmetric two-in-two-out arrangement has the lowest energy. Type II also has a two-in-two-out arrangement, but the adjacent magnets which are closer to each other compared to the opposing magnets are the ones that have their moments similar, yielding a slightly higher energy than type I. Type III has a three-in-one-out/three-out-one-in arrangement, while type IV has four-in/four-out. **(b)** The two-fold degenerate ground state is a tiling of type I vertices, resulting in loops of flux closure arrangements.

dipole interactions, even the lowest energy configuration in type I, with two moments in and two moments out, only minimize four out of six interactions (the two opposite magnets in the vertex have their moments head-to-head, or tail-to-tail).

Frustrated systems often portray a high degree of degeneracy, and no one true ground state [29]. This is the case for the well-known substance ice (frozen water) – from which parts of the term artificial spin *ice* has its origin – which has residual entropy down to absolute zero. The square artificial spin ice, on the other hand, has a well-defined two-fold degenerate ground state comprised of type I vertices, which is illustrated in Fig. 2.9b (where the degeneracy lies in that all the moments can be reversed leading to the same energy). The ground state can be described by the two sublattices (horizontal and vertical) both having an antiferromagnetic ordering of their macrospins, and being shifted relative to each other so that all vertices are type I. The depicted loops illustrate how the four magnets surrounding each loop have their moments arranged head-to-tail giving a flux-closure configuration.

Chapter 3

Simulation, Fabrication and Characterization Tools

The first section of this chapter deals with micromagnetic simulations and the simulation software mumax3. The two following sections presents the technique of electron beam lithography and the characterization tool magnetic force microscopy, which are the fabrication and characterization tools that have been employed in this thesis. According to [30], electron beam lithography and magnetic force microscopy are the two most important technologies of which the field of artificial spin ice has relied on. High-resolution nanopatterning is achieved with the use of electron beam lithography to create the magnets of the array. The magnetic force microscope gives access to the state of the ensembles, as one can resolve the magnetization of individual magnets. Another key characterization tool in the field of artificial spin ice, that should be mentioned for the sake of completeness, is that of x-ray photoemission electron spectroscopy (PEEM). Using PEEM, also enables the acquisition of the individual moments.

3.1 Micromagnetic Simulations in mumax3

Micromagnetic simulations are a valuable supplement to experimental activity. Simulations can be used as a mean to navigate the parameter space, and as a tool for interpreting and confirming experimental results. There are several micromagnetic simulation software packages available. In this thesis, the open-source, GPU accelerated mumax3 is utilized. The reader is referred to the website and paper[1].

In mumax3 the evolution of the magnetization in time and space is found, by numerically solving the LLG equation (Eq. 2.14). A finite difference method (as opposed to a finite element method) is employed, where space is discretized into a grid, and derivatives are replaced by finite differences. The grid is made up of space filling orthorhombic cells. The magnetization within the cells is assumed uniform, and each cell holds an associated reduced magnetization vector, $\mathbf{m}$ (Fig. 3.1). For this assumption to be appropriate the cell size used should not exceed the exchange length, l_{exch}, (Eq. 2.13) of the modeled material.

To store material parameters, each cell in the computational grid is assigned a region index. The relevant material parameters, like the saturation magnetization, the damping parameter and anisotropy constants are stored with the region index number. The cell grid, and a look-up table with material parameters are illustrated in Fig. 3.1. Different geometries of magnetic material (where the material type is defined by virtue of its region index) can be made by

[1] http://mumax.github.io, Arne Vansteenkiste et al. "The design and verification of MuMax3". In: AIP advances 4.10 (2014), p. 107133.

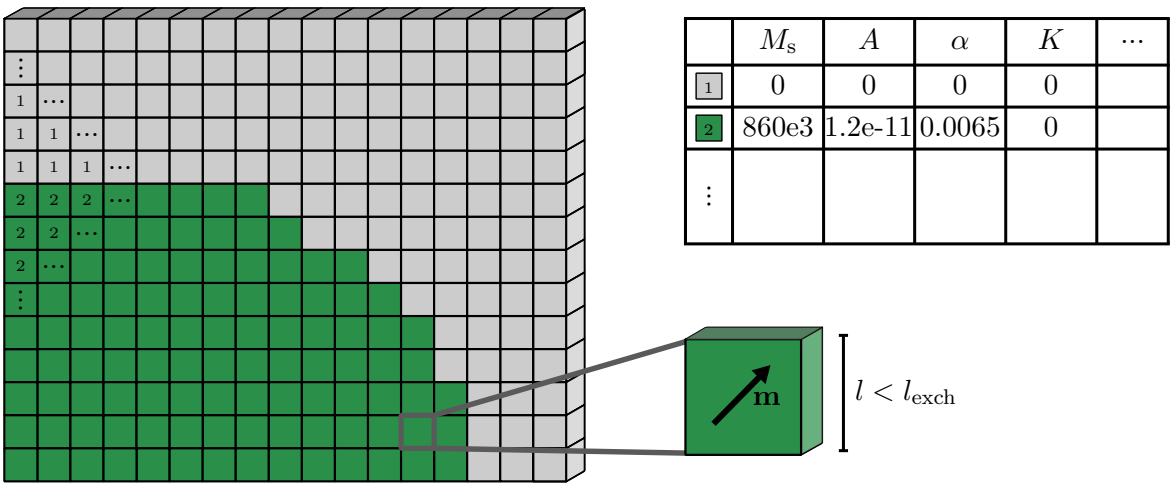

Figure 3.1: Illustration of the computational grid in mumax3 | The space is discretized into orthorhombic cells and each cell is assigned a region index to specify the material type. In this figure region 2 makes up magnetic matter while region 1 constitutes free space. Material parameters are stored with the region index number in a look-up table. The illustrated table contains the most important parameters that needs to be specified (it should be noted that the exchange stiffness, A, is not actually stored in the same table as the other parameters because it is a coupling parameter and is considered at the interface between the cells). The figure is adapted from [31].

using predefined shapes in mumax3, like rectangles and circles, and then move, rotate, scale and combine the shapes together.

The evolution of the reduced magnetization, $\mathbf{m}$, within each cell is calculated using an explicit form of the LLG equation,

$$\tau = \gamma \frac{1}{1+\alpha^2}(\mathbf{m} \times \mathbf{B}_{\text{eff}} + \alpha(\mathbf{m} \times [\mathbf{m} \times \mathbf{B}_{\text{eff}}])). \tag{3.1}$$

It can be shown that the equation above[2] is equivalent to Eq. 2.14 (see [32] for details). $\mathbf{B}_{\text{eff}}$ has contributions from the energy terms that were presented in the section on the micromagnetic energy terms (Section 2.2.1). Additionally, the effect of having a finite temperature can be incorporated by adding a fluctuating thermal field, $\mathbf{B}_{\text{therm}}$.

After having defined an initial magnetization state, the simulation can be `run(time)`, for a predefined duration in finite time steps (typically in the picosecond range). An alternative to the `run()` function is a `relax()` function which tries to find the energy minimum of the system, by disabling the precession term in Eq. 3.1.

A valuable extension provided by mumax3 is a magnetic force microscopy image generator, which produces an output image emulating what an experimentally retrieved image would look like. This extension is a valuable resource in interpretation of real magnetic force microscopy images.

[2]Several sources refer to the Eq. 3.1 as the Landau-Lifshitz-Gilbert equation, whereas the implicit equation given previously (Eq. 2.14) is termed the Gilbert equation.

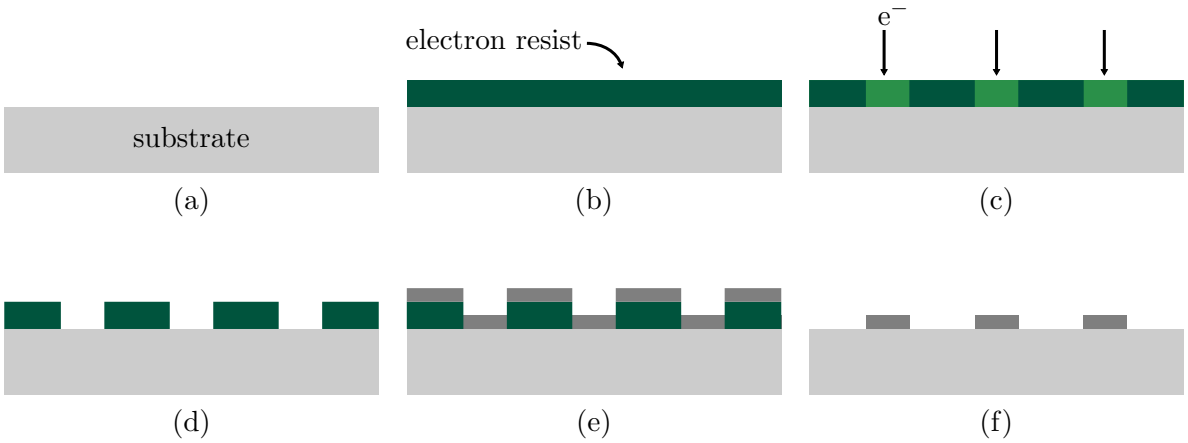

Figure 3.2: A schematic illustration of a fabrication process using electron beam lithography | **(a)** The substrate constitutes a planar surface to pattern on. A silicon wafer is a typical substrate. **(b)** A thin layer of electron resist is coated onto the substrate. **(c)** An electron beam exposes parts of the resist in a sequential manner. **(d)** When the sample is developed, the exposed part of the resist dissolves, leaving only the unexposed resist. **(e)** The wanted material is deposited onto the substrate. **(f)** Lift-off removes all the remaining resist and the material deposited upon it, and potentially tiny (nanoscale) free-standing features (magnets) are left on the substrate.

3.2 Fabrication with Electron Beam Lithography

Electron beam lithography (EBL) is the predominant technology used to make the nanoscale magnets of the artificial spin ices [30]. This section will, therefore, give a brief account of the technology and the associated fabrication process using EBL.

In general, lithography refers to producing a pattern on a substrate. The fabrication process of *photolithography* has been a prerequisite for the creation of integrated circuits (ICs) and continues to be at the heart of IC production, making it an invaluable technology in today's society. Photolithography involves the use of light (photons) to transfer a pattern, whereas electron beam lithography (EBL), uses – as the name suggests – an electron beam.

The workings of the EBL involve moving a focused beam of electrons across a sample covered with a layer of a polymer material called electron resist. The beam exposes the resist in a designated pattern, defined by a digital mask. When the electron resist is exposed to electrons, it changes chemically. The alteration of the exposed resist can either make it more or less soluble in a solvent known as a developer. Development of the sample, by placing it in the designated developer solution post-exposure, leaves a pattern in the resist caused by selective removal of either the exposed or un-exposed resist. Most often, one is interested in having a pattern of a material other than the resist, and there are therefore accompanying processing steps to achieve this. A typical fabrication process is illustrated in Fig. 3.2. After developing the sample, deposition of material can, for instance, be achieved with electron-beam evaporation. In the last processing step, the remaining resist is stripped from the sample in a process called lift-off, leaving a pattern of the wanted material as the final result.

Using electrons as the transfer medium, compared to photons, yields a great advantage in terms of resolution. EBL is considered to have the highest resolution among the different types of lithography [33], and features of sub 10 nm dimensions can be made [34]. For IC manufacturing, however, the sequential writing with the electron beam makes it too slow for large scale

production. In photolithography, the photons can, on the other hand, be shone onto the sample in a parallel fashion blocked by a physical mask, so that one can produce an entire pattern in a short amount of time.

3.3 Magnetic Force Microscopy

Magnetic force microscopy (MFM) is a high-resolution (around 50 nm [35]) characterization technique that probes and maps the vertical component of the magnetic stray field from a surface. The MFM belongs in the family of scanning probe microscopes (SPM), which are all based on measuring a specific interaction between a surface and a physical probe. The closest relative to the MFM is the atomic force microscope (AFM), which is used to determine the surface topography of a sample by probing the van der Waals forces between the sample and an atomically sharp tip placed on a flexible cantilever. What distinguishes the MFM from the AFM, is the use of a *magnetic* tip. The magnetic tip is influenced by, and thus able to probe, the magnetic field generated by the sample under investigation. To avoid mixing the magnetic information with topographic information the tip is lifted a certain distance above the sample, where the van der Waals interaction becomes negligible compared to the magnetic interaction (the van der Waals interaction energy has a r^{-6} dependence, while the magnetic interaction energy between two dipoles have a r^{-3} dependence (Eq. 2.4)).

An image is generated in the MFM by moving the tip over the sample (or, rather, the sample under the tip) while recording the tip-sample interaction. One can distinguish between two modes of operation. Conceptually, the most straightforward mode of operation is simply monitoring the deflection of the cantilever beam as it is either attracted or repelled from the sample stray field, as a function of position. This mode is what can be referred to as the static mode [36]. The static mode is, however, limited by a low sensitivity because of susceptibility to noise in the apparatus [37]. A more common mode of operation is thus a dynamic mode, where the cantilever is set to oscillate, at or near its resonance frequency, for instance by a piezoelectric actuator. The oscillation parameters (amplitude, frequency, and phase) of the cantilever are affected by the presence of a magnetic field. The phase change is the most common to record [35]. The oscillation at the end of the cantilever will exhibit a phase shift compared to the drive oscillation of the actuator. This phase shift is altered by the presence of a magnetic interaction between the tip and the sample and can be represented as an image of magnetic contrast. A schematic illustration of an MFM is provided in Fig. 3.3.

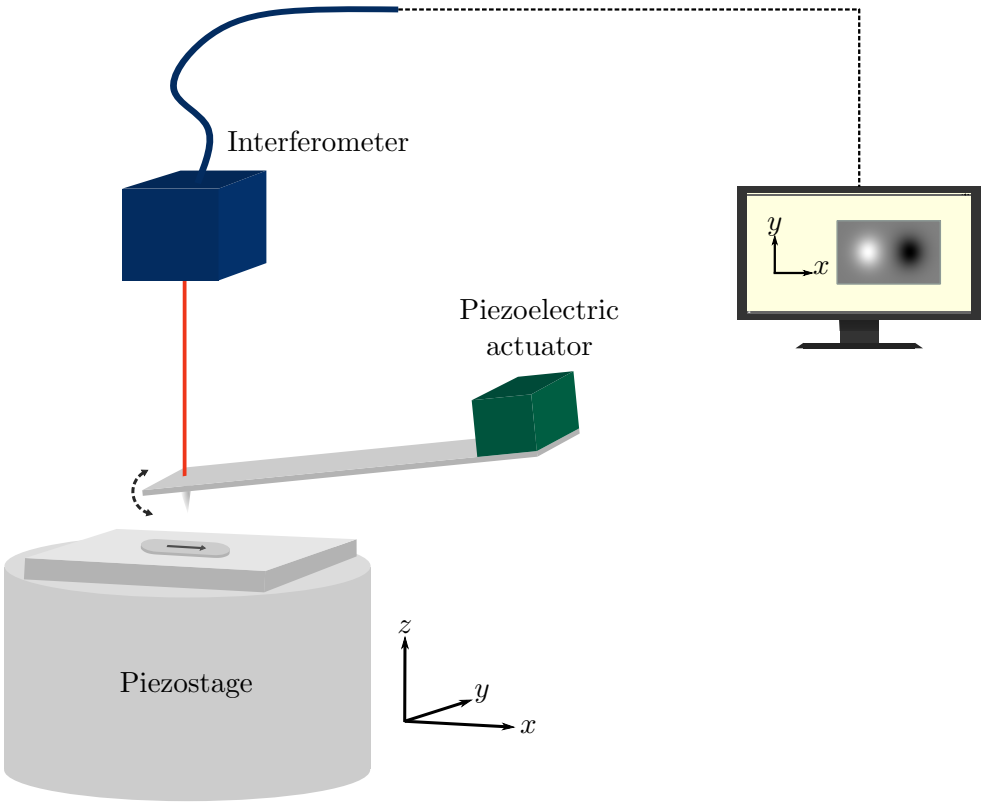

Figure 3.3: Illustration of the workings of a magnetic force microscope (MFM) | The magnetic material of the sample has an associated stray field with it that the magnetic tip interacts with. The piezo stage moves the sample under the tip. A laser interferometer is used to monitor the movement of the cantilever, which is driven to oscillate by the piezoelectric actuator. The tip will be attracted by the field at one end of the stadium magnet and repelled at the other, which gives rise to a different phase shift of the tip oscillation at the two ends of the magnet. These phase shifts are recorded and visualized in a contrast image.

Chapter 4

Experimental Procedure

The work of this thesis can essentially be divided into studies on three different systems. This chapter will therefore start by going through the *general* fabrication process, imaging, and the common simulation setup, before attending to the details of the separate studies. Firstly, a brief explanation of the sample fabrication is given, and the arrangement and geometry of the physically realized magnetic nanostructures that have been studied. Then follows a section on the magnetic force microscope which has been utilized, both technical specifications and the typical operation of the microscope. Subsequently, the general setup of the micromagnetic simulations is presented. Lastly, a more detailed procedure of the different studies is given.

4.1 Sample Fabrication and System Geometries

Three different types of systems – distributed on two samples – were studied: magnetic rings, single nanomagnets, and artificial spin ices with incorporated disk defects. The physical samples were fabricated at the NTNU NanoLab cleanroom facility by co-supervisor Anders Strømberg, and the procedure was the same in both cases. A roughly 100 nm thick layer of electron resist was coated on a silicon wafer. EBL was used to pattern the electron resist, in a procedure as outlined in Section 3.2. Electron beam evaporation was then used to deposit a 10 nm thick layer of polycrystalline permalloy (Py). In addition, a 2 nm layer of aluminum was deposited to function as an oxidation barrier. The final processing step was lift-off.

Scanning electron microscopy (SEM) images of the three systems are shown in Fig. 4.1. The geometry of the Py rings were defined according to a matrix with an increasing radius when moving up, and an increasing thickness of the ring towards the right in Fig. 4.1a. The nanomagnets, both the single ones and those in the artificial spin ices, are stadium shaped with an overall length $l = 220\,\text{nm}$, a width $w = 80\,\text{nm}$, and a Py thickness of 10 nm. For the artificial spin ice systems, the pitch of the lattice and the diameter and location of the included disk defect are also important geometry parameters.

4.2 Imaging with the Magnetic Force Microscope

This section describes the technical specifications of the MFM, the general start-up routine, and imaging considerations that needs to be taken.

4.2.1 System Specifications

The MFM used in this project is an AttoAFM/MFM I, manufactured by Attocube systems. The MFM is operated in the dynamic mode, with phase change detection. The cantilever tip is of type MFMR-10 from NanoWorld, coated by a cobalt alloy to ensure a magnetic moment.

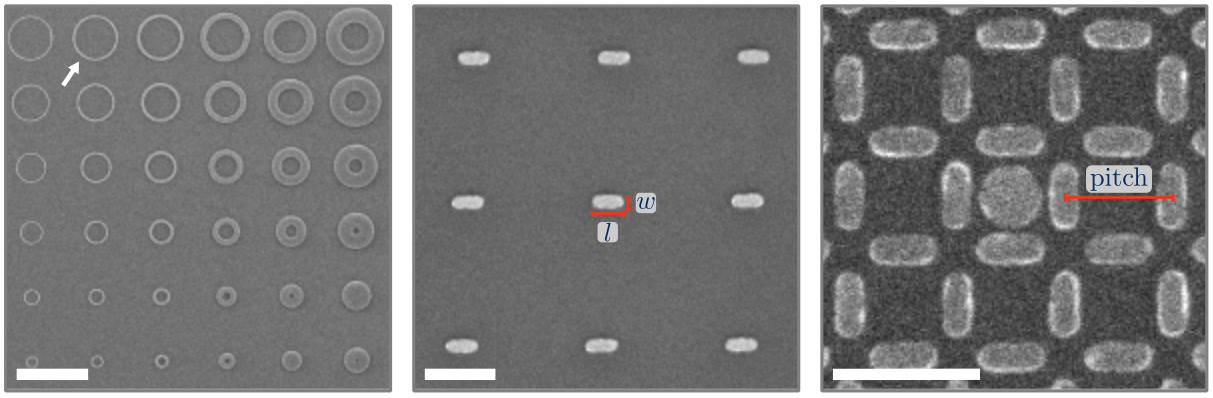

(a) (b) (c)

Figure 4.1: SEM images of the three studied systems | **(a)** 10 nm thick Py rings with varying dimensions. The arrow marks the ring that was focused on, which has an inner radius of 1.16 µm and an outer radius of 1.24 µm. The scale bar is 4 µm. **(b)** Single nanomagnets placed with a 1 µm distance between them. These nine magnets are a small piece of an array with several thousand similar ones. The length and width of a single stadium magnet are marked on the figure. The scale bar is 500 nm. **(c)** A small section of a square artificial spin ice with an added disk defect. The pitch is the center-to-center distance as illustrated on the image. The scale bar is 500 nm.

Table 4.1: Parameters of the two MFMR-10 cantilever tips used as specified by the manufacturer. The parameters are thickness, T, width, W, length, L, spring constant, C, and resonance frequency, f.

T [µm]	W [µm]	L [µm]	C [N/m]	f [kHz]
3.4	28	223	4.1	84
3.4	28	223	3.7	81

The tip parameters are listed in Table 4.1. Cryogenic temperatures are achieved by placing the microscope in an AttoDry1000 XL cryostat. The cooling power of the cryostat cannot be adjusted, so to achieve a stable temperature a small heating element can be controlled with a feedback loop. A magnetic field, in the sample plane, of varying strength is produced by a superconducting 5 T split coil electromagnet placed inside the cryostat. The cantilever movement is detected using an optical fiber-based interferometer, with a 1310 nm wavelength laser. Mounting of the sample on the microscope is done using both a small droplet of silver-based adhesive and copper tape, in order to ensure electrical contact between the sample and the grounding plate to which it is mounted. A piezoelectric stack enables precise movement of the sample.

4.2.2 Temperature

The MFM images presented herein were captured at cryogenic temperatures, to make use of the superconducting magnet which must be held at temperatures below 9.8 K to be operational. According to manufacturer instructions, prior to immersing the microscope within the cryostat, the cryostat needs to be pumped down to a pressure of approximately 20 mbar, then filled with 20 mbar of helium gas and cooled to sub 5 K. This practice was followed every time the tip or sample was changed, which involves removing the microscope from the cryostat and immersing it anew. The aforementioned heating element was utilized to keep the temperature stable at 8 K under the acquisition of all the experimentally retrieved images presented.

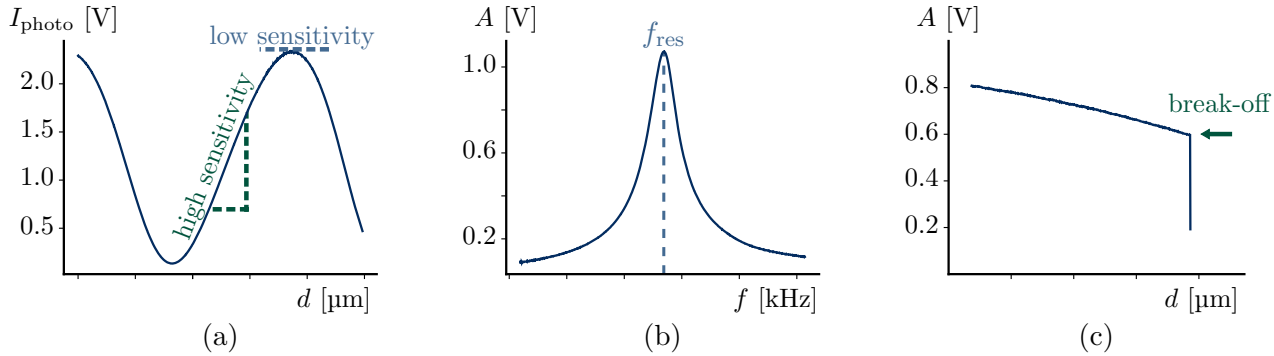

Figure 4.2: Calibration curves for finding operating parameters | **(a)** A typical spectroscopy plot retrieved to determine the distance between the end of the optical fiber and the cantilever. The highest sensitivity for monitoring the cantilever movement is obtained when the distance corresponds to the part of the plot with the largest slope. **(b)** The oscillation amplitude of the cantilever tip in response to an AC voltage at varying frequencies. The peak of the curve corresponds to the resonance frequency of the tip. An AC voltage with the resonance frequency determined from such a plot is applied to drive the cantilever. **(c)** The oscillation amplitude of the cantilever tip as the separation between the tip and the sample is decreased. The abrupt decline happens at the break-off voltage, due to the onset of van der Waals forces.

4.2.3 Calibrating the Microscope for Imaging

Prior to each imaging session (in both cryogenic and room temperature operation) the microscope needs to be calibrated, a process involving roughly three steps. First, the sensitivity to cantilever deflection is maximized by adjusting the interferometric path for the laser. A piezoelectric actuator controls the distance between the outlet of the optical fiber and the cantilever. Applying a range of voltages to the piezo actuator and measuring the self-interference amplitude results in a plot like the one in Fig. 4.2a. The operating voltage is chosen to be at the value where the plot has the largest slope (between two extrema values) and thus also has the highest sensitivity to cantilever deflections. Second, the resonance frequency of the cantilever is found, and the cantilever is set to oscillate at this frequency, by inducing an additional small AC voltage to the same piezoelectric actuator as before. The resonance frequency is determined by applying an AC voltage at different frequencies (70 kHz to 90 kHz for the tips used in this thesis) and plotting the response from the cantilever oscillation amplitude (Fig. 4.2b). The characteristic peak corresponds to the resonance frequency of the cantilever. The final step is to determine what is denoted the break-off point. The distance between the sample and the cantilever is slowly decreased. At a particular separation, the onset of van der Waals forces creates an abrupt decline of the cantilever oscillation amplitude. Fig. 4.2c shows a typical curve for retrieving the break-off point, and the oscillation amplitude where the sudden decline happens is the break-off voltage, as marked on the figure. As a rule of thumb from the manufacturer, an amplitude of 0.8 times the break-off voltage corresponds to contact-mode. A feedback loop is used to fix the tip at this amplitude, by continuously adjusting the sample height. AFM scans are performed in the contact mode, whereas for MFM scanning the tip is lifted a certain height away from the contact mode, to separate the magnetic forces from the Van der Waals forces.

4.2.4 Imaging Parameters

A few image parameters can be altered that significantly affect the quality of the retrieved MFM images, and these parameters are typically adjusted often. It should however be noted that more important than the image parameters for the retrieved image quality is the condition of the tip. The resonance curve (Fig. 4.2a) can often give an idea of whether the tip is in good shape or not. Several resonance peaks will, for instance, be an indication of a tip below par.

Another deficiency is the tip having a double apex, which results in images with features that appear twice. When the tip, on the other hand, is satisfactory, the most critical parameter is the lift height, which refer to how much the tip is lifted away from contact mode. The further away from the sample surface one is probing the field, the weaker the stray field from the sample is. Additionally, the field from different parts of the sample overlap to a larger extent, which makes it hard to resolve the magnetic state. Resolving the magnetic state of the sample is often much easier with a low lift height. However, as the tip is magnetic, if it is brought too close to the sample, it might become invasive and alter the magnetization of the sample. A possible consequence of a tip that is brought too close to the sample is shown in Fig. 4.3a. In the middle image, where the lift height of the tip is 25 nm, the magnetization of the top magnet is reversed because of the tip as it scans over the magnet, effectively changing the magnetization state of the sample. A second parameter that must be chosen and optimized is the speed of the tip as it sweeps over the sample[1]. A high scan speed results in images with features that appear to be smudged out, because the excitation of the tip by interaction with a sample feature is not damped fast enough. The effect of scan speed is illustrated in Fig. 4.3b. Finally, the pixel size is set by determining the number of scan lines (the tip scans the sample in a meander scan scheme). For the images presented here, the parameters are chosen as a compromise between image quality, risk of altering the magnetic state, and a reasonable scan time. The lift height for the images presented is typically in the range 60 nm to 90 nm and will be specified.

4.3 Simulation Setup

The software package mumax3 is employed for the simulations. The material parameters used are standard values for Py, with the saturation magnetization, M_s, equal to 860×10^3 A/m, the exchange stiffness, A, equal to 1.2×10^{-11} J/m, the dimensionless damping parameter, α, is set to 6.5×10^{-3}, and the crystalline anisotropy is 0 (which, coincidentally, happens to be exactly the same values as those in the table in Fig. 3.1). The cells surrounding the magnets are not magnetic and constitutes free space. Temperature is not included. The in-plane cell size utilized in all simulations is 2 nm × 2 nm. The exchange length of Py is 5.1 nm [38] (this value can be calculated from the material parameters given above using Eq. 2.13), hence the cells are sufficiently small. Because we expect there to be no out-of-plane magnetization for the thin film structures, we can save ourselves from extra computational cost and have only one cell in the z-direction, with the same length as the height of the Py thin films; 10 nm.

4.4 Experiment Overview

This section contains a more detailed description of sample geometries, and the procedures undertaken both in the experimental work and in simulations.

4.4.1 Magnetic Rings

To investigate whether rings of Py could be used as a "compass" to pinpoint the direction of the magnetic field on the sample, several of the rings in the matrix in Fig. 4.1a were imaged after application of positive and negative fields of varying strength. The arrow on the figure points at a ring that seemed to show the desired response, where the dimensions are inner radius of 1.16 µm and outer radius of 1.24 µm, giving an 80 nm thick ring. This ring was imaged after experiencing varying fields. The microscope was at one point rotated approximately 15° clockwise from its standard position and the ring was imaged after experiencing ±80 mT.

[1]The tip is in reality held still; the stage is moved under the tip.

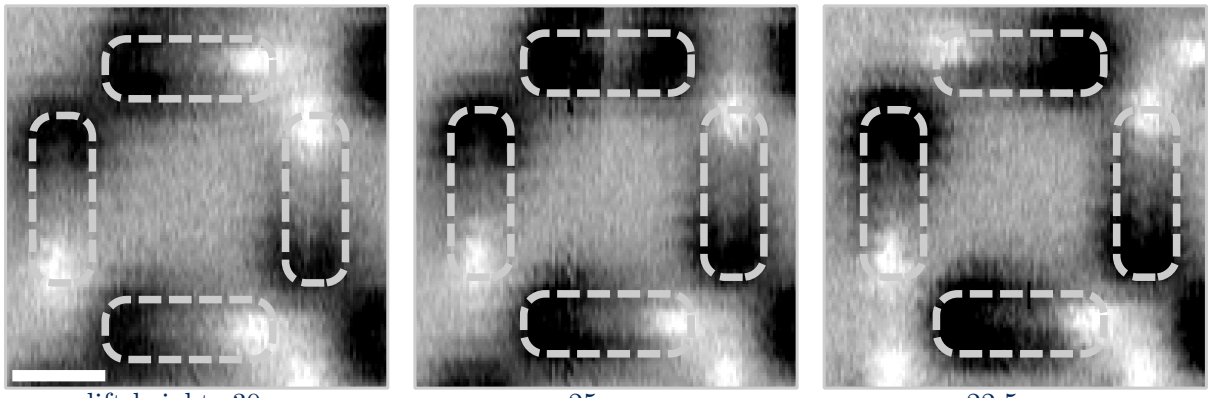

(a)

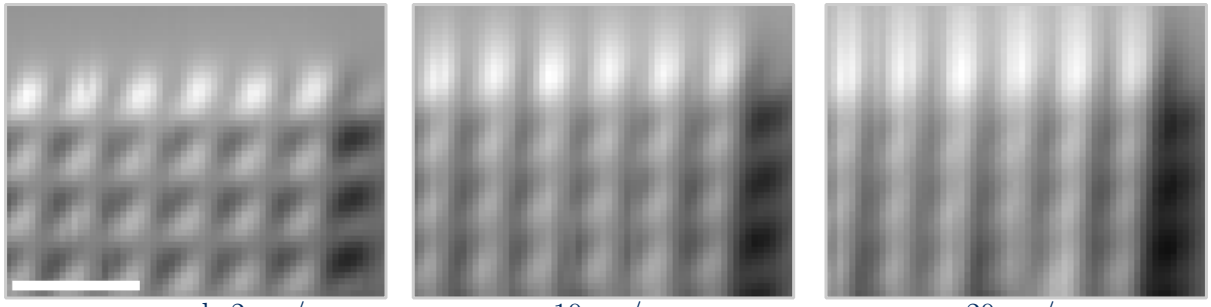

(b)

Figure 4.3: The choice of image parameters when operating the MFM is important[2]| **(a)** These images show what could potentially happen if the lift height of the tip is too low. When the lift height is decreased from the first to the second image, the magnetization of the top middle magnet is flipped while it is scanned over, which results in an image where both ends has a black contrast (which would correspond to a magnetic monopole). The third image shows that the top magnet did indeed reverse its magnetization, as we see that the direction of the magnetization is altered from the first to the third image. The lift height is in fact slightly decreased from the second to the third image as well, however the tip does not induce any switching in the third image. A possible explanation is found in the arrangement of the four magnets, which can be recognized as a flux closure configuration, i.e. ground state ordering. The scale bar is 200 nm. **(b)** The three images illustrate how an increase in scan speed impacts the captured images. The scan speed is the only parameter that is altered between the three images, that depict the top right corner of a square artificial spin ice. The scale bar is 1 µm.

[2]The images presented in this figure were taken during the fall of 2019, as part of the specialization project.

Micromagnetic simulations of a ring structure with identical geometry as the physical one was carried out. A field of ±80 mT was applied at different directions, before the ring was relaxed in zero field. The magnetization states were saved, along with simulated MFM images made with the MFM generator provided by mumax3.

4.4.2 Single Nanomagnets

In total 2100 different nanomagnets, arranged on a lattice with a 1 µm distance between every magnet (Fig. 4.1b), were imaged after application of consecutive field steps to determine the distribution of switching fields. Because there is a limited scan range in the MFM, this process had to be repeated on different areas of the large array of single magnets. The magnets were saturated with a −60 mT field (at approximately 45° to the long axis of the magnets), before the field was reversed and 40 mT to 51 mT was applied with 1 mT steps. Between each step the field was lowered back to zero and the system was imaged. The number of flipped magnets after every incrementation of the field was counted using imageJ[3] to identify the difference in the images taken between two consecutive field steps.

4.4.3 Disk Defects in Artificial Spin Ice

Initial simulations were run to determine parameters of interest. A system of 60 nanomagnets was used for the simulations, and a disk defect of varying diameter with the same material parameters and the same thickness as the elongated magnets was included in the simulation array. The disk was placed in a non-symmetric location (i.e., not in the middle of the ensemble) in between four magnets as shown in the physically realized artificial spin ice with a disk in Fig. 4.1c. To investigate the switching behavior of the ensemble, the array was first initialized in a polarized state with solely type II vertices, with vertical magnets magnetized upwards and the horizontal magnets magnetized towards the left. A field was applied in the opposite direction to the net magnetization of the array and increased from 0 mT to 36 mT using the `run()` function for 10 ns. From 36 mT to 51 mT the field was incremented in steps of 1 mT. At each field strength the `run()` function was utilized for a duration of 5 ns, as initial simulations revealed that the dynamics of the system had mostly disappeared within that time, while the incrementation of 1 mT was done with `run()` for 1 ns. The magnetization state of the ensemble was saved after 5 ns at each field, before incrementation. Simulations with varying pitches of the array and an added disk with 200 nm in diameter were conducted with the same procedure.

A set of geometries were physically fabricated. Ensembles of 60 magnets similar to some of the simulated geometries were made. Some larger ensembles with 1300 magnets were also fabricated, with zero, three or five disk defects added in the lattice (Fig. 4.4). The switching characteristics of two small ensembles with a pitch of 340 nm and 350 nm were experimentally investigated. The ensembles were both saturated in the polarized state similar to the simulated initial state by applying a sufficiently large and negative field of −60 mT, before a positive applied field was incremented in steps of 1 mT. The field was, after each incrementation, reduced to zero, and the ensembles were imaged at remanence. The same procedure of saturating the array and incrementation with positive fields was repeated twice for both pitches. From the experimentally retrieved images of the small arrays, the magnetization states were decoded (with a combination of educated guesswork, and trial and error). To verify whether the states were correctly interpreted, the MFM image generator in mumax3 was made use of. Simulation geometries similar to the physical arrays, but without the disk, were made. By manually setting the magnetization direction of each magnet and simulate what the corresponding MFM image would look like, the decoded states could be verified. It should be stressed that the simulated MFM

[3] https://imagej.nih.gov/ij/

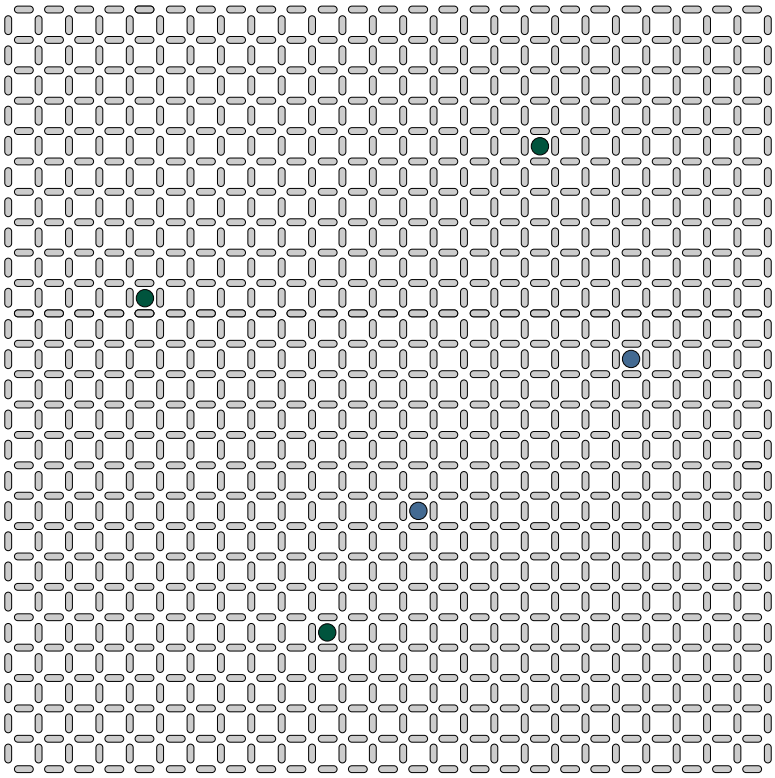

Figure 4.4: The layout of the large artificial spin ice with embedded disks | The disks are randomly distributed in the array, consisting of 1300 magnets. The arrays with three embedded disks have disks placed on the locations of the green colored circles. The arrays with five disks have them located as shown with all the circles (both green and blue).

images resulting from this procedure, do not correspond to any true micromagnetic simulations.

The larger ensembles were also imaged in the MFM. Prior to applying any magnetic fields to the sample, the large ensembles with three varying pitches and zero, three and five disk defects were imaged. Additionally, the large ensembles with five embedded disks were also imaged to investigate the switching of the magnets. Similar to prior, the ensembles were saturated with a sufficiently large and negative field, before the field was incremented, in steps of 1 mT, in the opposite direction. After each incrementation the field was reduced to zero and the ensembles were imaged at remanence.

Chapter 5

Results and Discussion

In this chapter, the retrieved results from the three studied systems – magnetic rings, single nanomagnets, and artificial spin ices with added disk defects – will be presented and discussed separately. The first section contains the results from MFM imaging and simulations of the magnetic ring. The following section presents the results from the study of the single nanomagnets. Finally, the results from the study on artificial spin ice systems with an embedded Py disk are presented and treated.

5.1 Magnetic Onion State as a Compass

In order to verify the direction of the applied magnetic field experienced by the samples, an experiment was conducted to determine two things. First, is it feasible to use a ring structure of Py to pinpoint the applied field direction by imaging the response of the ring? Second, if the former turns out to be so, what is the direction of the applied field?

Micromagnetic simulated MFM images of a ring with the same dimensions as the accentuated ring in Fig. 4.1a are given in Fig. 5.1. The simulated images are "captured" at remanence, after applying a field of 80 mT at varying angles counterclockwise from the vertical axis as shown in the figure. Superimposed on the images are illustrations of the magnetization state as obtained by the simulations. Experimentally retrieved MFM images of the accentuated Py ring in Fig. 4.1a after experiencing a field strength of ±80 mT are shown in Fig. 5.2a and c. The experimental images are also taken at remanence. Next to each of the experimental images, simulated MFM images of the ring, after a field of 80 mT in the direction shown with the arrows, are given. The same black and white features, that correspond to opposite phase shifts, are present in all images. Moreover, in the simulated images, where we are certain of the direction of the

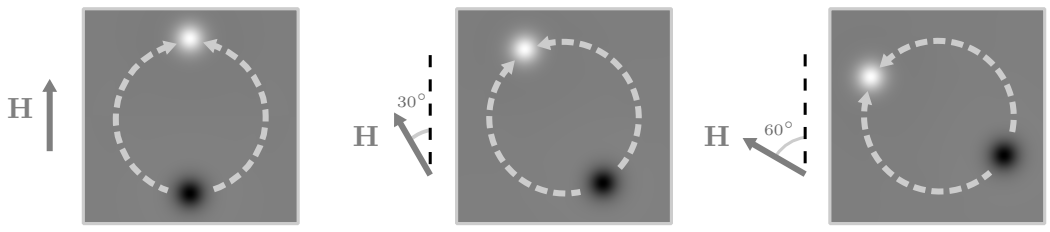

Figure 5.1: Simulated MFM images with varying directions of the applied field | A field of 80 mT was applied at angles 0°, 30° and 60° counterclockwise from the vertical axis, before the ring was relaxed in zero field. The circular arrows illustrate the magnetization state, retrieved from the simulations. The white and black contrast are one head-to-head and one tail-to-tail domain wall.

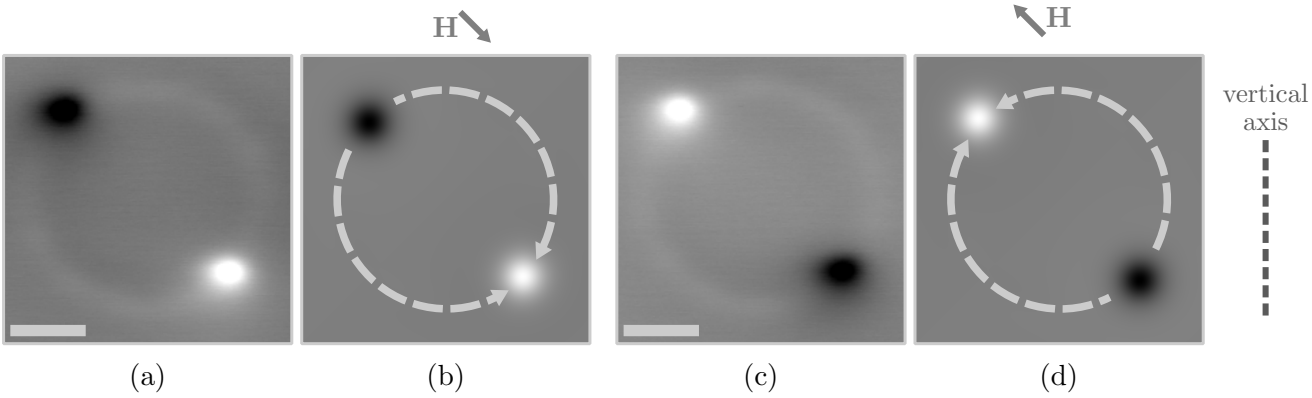

Figure 5.2: Experimental and simulated MFM images of the Py ring | **(a)** Experimentally captured MFM image after exposing the sample to a field of 80 mT and lowering it back to zero. **(b)** Simulated MFM image after applying 80 mT and then relaxing the ring in zero field. The direction of the simulated field is indicated above the image and is at an angle of 45° counterclockwise from the vertical axis. **(c)** Experimental MFM image after a reversed field compared to in **(a)**. **(d)** Simulated MFM image with a reversed field compared to **(b)**. The scale bars on the experimental images are 1 µm. The lift height is 120 nm. The dimensions of the simulated ring are the same as the physical one, with inner radius of 1.6 µm and outer radius of 1.24 µm.

field that was applied, the black and white features are aligned with the axis of the field.

The appearance of both the experimental and the simulated MFM images can be explained by the ring having a magnetization state known as an onion state [39]. In ferromagnetic rings, magnetostatic energy favors a circulating magnetization. A magnetization that circulates completely around, either clockwise or counterclockwise, and bites its own tail corresponds to a vortex state. Upon applying a magnetic field, the Zeeman energy prefer alignment of the magnetization with the field. When the field is lowered again, the remanent state will typically be the onion state, which is two halves – domains – of oppositely circulating vortex states. The two magnetization domains are separated by one head-to-head and one tail-to-tail domain wall between them. These two domain walls are what we see in the MFM images, as they are a source of vertical stray field that the tip interacts with. The magnetization elsewhere circulates along the circumference of the ring and produces negligible stray field. In the simulated MFM-images the rest of the ring, apart from the domain walls, produces no observable contrast. In the experimental images we can, however, make out a weak ring contour. The two domains of the onion state will be mirror symmetric about the axis of the applied field, and the axis is easily recognized by the two domain walls. In that sense, the ring demonstrates compass-like properties, which was exactly our sought-after property.

Using the identified compass properties of the ring, the direction of the field within the cryostat can be determined by the experimental images in Fig. 5.2a and c. The white and black feature in the experimental images are located on an axis close to 45° counterclockwise from the vertical axis. Additionally, the experimental images look very much alike their simulated counterparts placed beside. We can therefore pinpoint the direction of the field in the experiment to be like in the simulated case, that is, 45° counterclockwise from the vertical axis. It should be noted that the experimental images in Fig. 5.2 were captured after having rotated the microscope approximately 15° clockwise from its standard position. The direction of the field in the standard position is thus pinpointed to 30° counterclockwise from the vertical axis. An illustration of the microscope, its rotation and the applied field direction is given in Appendix A. Images of the

ring structure were also captured prior to rotation of the microscope and verified this. Having acquired this knowledge, we can continue on the next sections with a strengthened confidence on the direction of the applied field.

5.2 Quantifying the Quenched Disorder

The switching field of 2100 magnets were sampled by incrementation of an applied magnetic field 45° to the long axis of the magnets, and imaging between consecutive field steps. The aim was to quantify the spread in switching fields of the magnets, as a consequence of imperfections and variation from the fabrication.

A histogram plot presenting the distribution of switching fields is provided in Fig. 5.3. Each bar of the histogram represents the number of magnets that have reversed their magnetization at the corresponding value of the applied magnetic field. Of the 2100 magnets that were sampled, there is a total span in the switching field of 11 mT, from 40 mT to 51 mT. Superimposed on the experimental data is a curve fitted normal distribution, which has a standard deviation of 1.8 mT, and an expectation value of 46 mT. A selection of the images used to make the histogram plot is given in Fig. 5.4, where excerpts of some of the captured MFM images belonging to one image series (one repetition of field incrementation and imaging) are shown. A full image series, where the differences between subsequent fields are highlighted, are given in Appendix B. The leftmost image is taken after application of −60 mT[1], and all the magnets are magnetized in the same direction, with white contrast on the left side and black on the right.

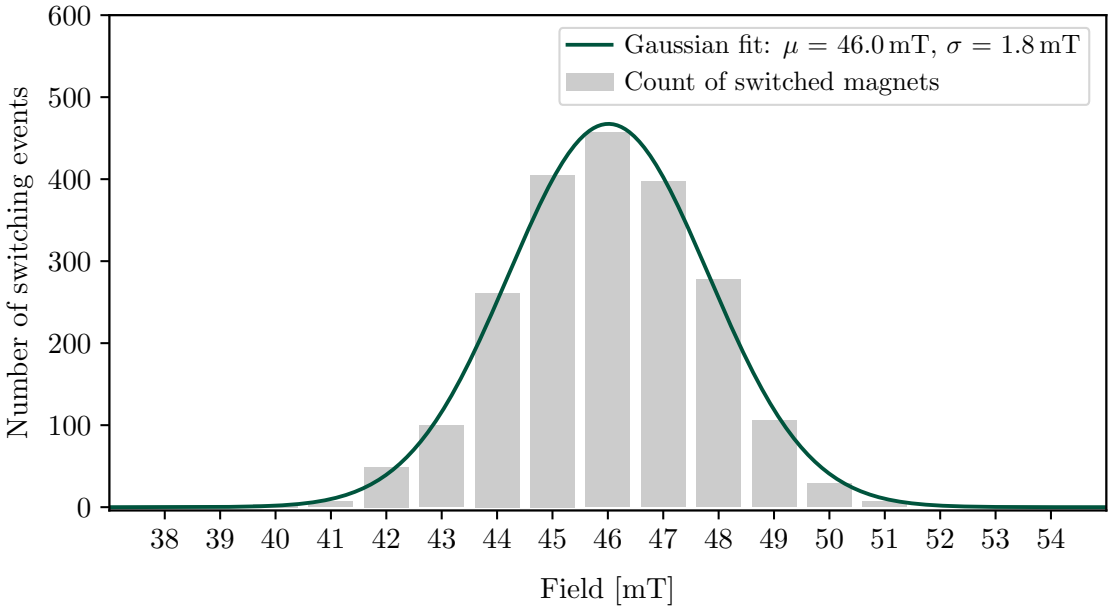

Figure 5.3: Experimental distribution of the switching field for the single nanomagnets | The histogram presents a switching field distribution retrieved by determining the switching field of 2100 magnets at 8 K, with a field applied 45° to the long axis of the magnets. The height of the bars gives the total number of switched magnets at the corresponding value of applied field. A normal distribution is fitted to the experimental data. The fitted curve has a standard deviation of 1.8 mT and an expectation value of 46 mT.

[1]The direction of the field was determined in the previous section (Section 5.1), and the microscope is rotated similarly to in Fig. 5.2. When giving a negative field value it corresponds to a field in the direction of the leftmost arrow in Fig. 5.4, and a positive field is meant to denote a field in the opposite direction.

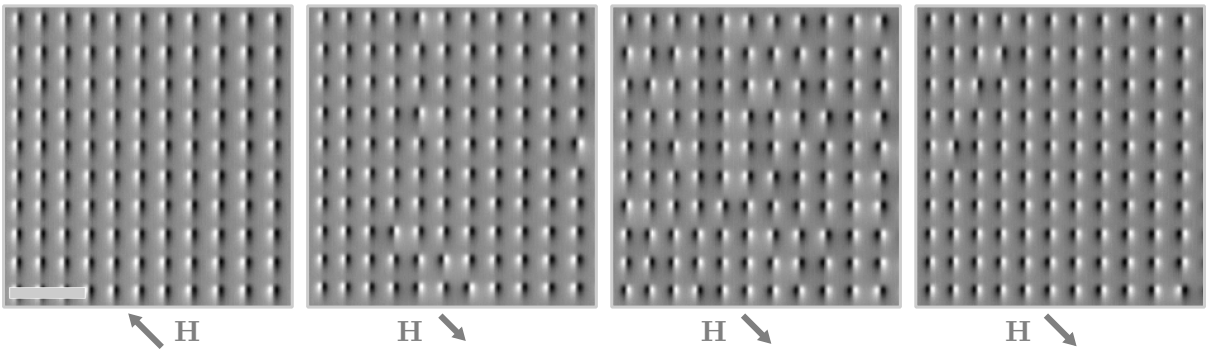

Figure 5.4: MFM images of the single nanomagnets after different applied fields | The leftmost image is captured after application of −60 mT. We see that the all the magnets have white contrast on the left end, and black contrast on the right, and they are thus magnetized in the same direction. This division into a black and white end also verifies that the magnets are single domain. In the next image, the field has been reversed, and the sample has experienced 43 mT in the direction indicated by the arrow. Nine of the magnets included in this image have reversed their magnetization, which can be seen from an interchange of which end that has white and black contrast. The next image is taken after applying 46 mT, and now several switches have occurred. The rightmost and last image shows the state of the array after being exposed to 49 mT, where almost all the magnets have switched. The lift height in all images is 90 nm. The dimensions of the images are equal, and the scale bar on the leftmost image is 3 µm.

The second image is captured after 43 mT, and we see that a few of the imaged magnets have flipped their magnetization, which is seen from a reversal of the white and black contrast of some of the magnets. Increasing the field further results in about half the magnets having switched on the next image, before finally after 49 mT, in the last image, almost every magnet is switched.

In experimental work, we are forced to deal with the real world (in contrast to an ideal world). Imperfections from the nanofabrication of the magnets are inevitable. There will be small variations in patterning, in the metal deposition and in post-fabrication oxidation. In a physical sample, there will thus be slight variations in the dimensions and in the edge roughness of the nanomagnets that tile the substrate. In the field of artificial spin ice, these imperfections are often referred to as a quenched disorder – the disorder is "frozen" in the geometry. The properties of a nanomagnet are intimately connected to its volume, its shape and to the presence of surface asperities [17]. As we expect there to be a variation in these parameters among the fabricated magnets, we expect, as a consequence, a variation in the properties of the magnets, and more specifically a variation in the *switching field*. Evidently, this is what we see from the histogram plot in Fig. 5.3, where the variation in the switching field can be quantified by the standard deviation of the fitted normal distribution, i.e., 1.8 mT.

The aim was to quantify the spread in switching field caused by fabrication imperfections. Can we trust that this is what the retrieved value of the spread reflects? For one thing, the tip has the potential to become invasive and cause reversals of the magnets while we are imaging, as was shown in Fig. 4.3a. Imaging of the single nanomagnets was done in zero applied field, in order to avoid that the stray field from the tip in addition to an applied field would amount to the switching field of the magnets. Moreover, the lift height of 90 nm used under the acquisition of the images in Fig. 5.4 (and in all other images captured to make the plot in Fig. 5.3) is fairly high. Inspection of the images did not reveal any monopole-looking magnets. Furthermore, there was a finite temperature of 8 K present, which contributes with a certain

amount of thermal energy. The thermal energy alone could cause an apparent spread in the switching field for the magnets, because with assistance from thermal energy a magnet might be able to reverse its magnetization if the applied field is *close to* the switching field (Fig. 2.8b). However, the difference in Zeeman energy experienced by a single magnet when the applied field is incremented by 1 mT is on the order of 1 eV, whereas the thermal energy at 8 K is thousand times smaller, at around 1 meV. The role of temperature on the observed values of the switching fields is thus limited. Whether the applied field values correspond to the true switching field also depends on the validity of the assumption of non-interacting magnets. If the distance of 1 µm between the magnets is not sufficient, they will be exposed and affected by the dipolar fields of the surrounding magnets, which would affect the size of the applied field necessary to switch the moments. The dipolar interaction energy between two magnets with a 1 µm separation is roughly 20 meV, potentially making it more significant than the thermal energy. However, the dipolar interaction is small in comparison to the change in Zeeman energy when incrementing the applied field with 1 mT.

We can compare the standard deviation in the switching field found here with other values presented in the literature. Ladak et al. [40] studied a connected artificial spin ice (the magnets are physically linked together) with a honeycomb geometry. To account for the disorder and make simulated results agree with experimental ones, they used a normal distribution for the switching field of the individual magnet bars in their simulations, with a standard deviation of 10 mT, relative to an expectation value of 60 mT. This value for the standard deviation is considerably higher than what we find here. The magnet bars were in that study, however, of quite different dimensions (length of 1000 nm, a width of 100 nm, and a thickness of 20 nm). Moreover, the magnets were fabricated from polycrystalline cobalt. According to [41], thin film elements fabricated from polycrystalline cobalt is expected to have a broader distribution of switching fields because of a strong (hexagonal) magnetocrystalline anisotropy, making the direct comparison inapt. Another study by Pollard et al. [42] on the square artificial spin ice, with Py as the magnet material, report on a standard deviation of 6 mT relative to a mean of 32 mT to model the disorder. These values are along the long axis of the magnets. Again, there is an appreciable difference from what is retrieved here. The magnets in that study also had magnet dimensions (100 nm-wide, 300 nm-long, and 30 nm-thick) quite different from ours. Magnets with the same length, and width as the ones here, and a thickness of 25 nm are studied by Kohli et al. [43]. By incorporating the island edge roughness that they retrieve from SEM images directly into micromagnetic simulations, they find that the disorder in the nominally identical magnets makes the coercivity vary with approximately ±8 mT. The width of the fitted normal distribution here is roughly 12 mT, giving a comparable value of ±6 mT in our case.

Irrespective of whether our retrieved value for the spread in switching field is lower, higher or comparable to other fabricated samples, it is there. The presence of disorder, and its extent, do affect the behavior of artificial spin ice arrays [15, 41, 43, 44]. For modelling and simulation of these arrays, a reliable experimental estimate of the extent of disorder is therefore important. Moreover, if one wants to add perturbations or tailored defects into the arrays, knowledge on the inevitably present disorder from fabrication is needed. In that way, one can make sure that the effect of the perturbation one is adding is more pronounced than the effect of the already present variation in the switching field. With that in mind, we can continue to the next section, where indeed an attempt at introducing a tailored defect is made.

5.3 Disk Defects in Square Artificial Spin Ice

> "No magnet is an island entire of itself; every magnet is a piece of the array, a part of the main."
>
> John Donne, 1624, slightly revised[2]

Moving away from the arrays of magnets with a separation presumably sufficient to ensure that they are indeed *islands entire of themselves*, we turn to the artificial spin ices, where the magnets are not, they are coupled. This section is devoted to the square artificial spin ice with one or more Py disk defects added in the array. Firstly, captured images of the as-grown state of several ensembles prior to any deliberate exposure to magnetic fields are treated. Subsequently, both simulated and experimentally retrieved results on the switching characteristics of artificial spin ices with embedded disk defects are presented and discussed.

5.3.1 Domains

MFM images of artificial spin ice ensembles with zero, three and five added disk defects, and three different pitches are shown in Fig. 5.5. The location of the disks in the arrays are as illustrated in Fig. 4.4. The ensembles have not experienced any (deliberate) global magnetic fields. It is difficult to see any traces of the disks embedded in the ensembles in the images of column two and three. What we on the other hand do see, are large areas of a repeating pattern with a low contrast in all the images. On this background, there are string features and localized smaller features of higher contrast. The low contrast pattern is a tiling of type I vertices, whereas the higher contrast elements are mainly type II and III, and less likely type IV vertices [45]. A few instances of type IV vertices are nonetheless observed by close inspection. The connected string features are referred to as Dirac strings[3] [15]. The leftmost image in the second row (regular 350 nm-pitch artificial spin ice) has a distinct black patch in the image, which is a consequence of incomplete lift-off in that area.

The appearance of the images is a testament to the coupled nature of the magnets. To minimize the dipolar interactions the island moments form domains of ground state ordering (Fig. 2.9b). Because of the two-fold degeneracy of the ground state, there will be a formation of both types. The strings, which make up the domain walls, are formed where the out-of-phase ground states meet. The size of the domains is expected to decrease with an increasing pitch, because the dipolar interactions decrease [46]. Examining our images, this seems to be the case. No considerable distinctions are detected between the images of the first and second row, where there is a 10 nm difference in the pitch. Comparing the last image row of the 370 nm-pitch arrays, however, with the two above one could claim that the domain size is smaller. There also seems to be a larger population of localized groups with moments deviating from the ground state in the last image row, especially prominent in the leftmost image, which makes it hard to define the limits of connected domains.

The moments of our array can be considered frozen, they are not fluctuating. A possible explanation for the ordering is thus that it took place in the course of the fabrication process [45]. During the deposition of Py, the magnets will start out with a very small thickness, which increases as more material is deposited. The switching barrier in Eq. 2.15 is lowered with a smaller volume, and so we can image the moments to be thermally active at sufficiently small

[2] To recreate the original version, exchange "magnet" with "man" and "array" with "continent".

[3] Named after British physicist Paul Dirac. The Dirac strings in artificial spin ices are emergent properties of the array, and not a Dirac string in the true sense as proposed by Dirac, that is, a flux string connecting two fundamental magnetic monopoles [15].

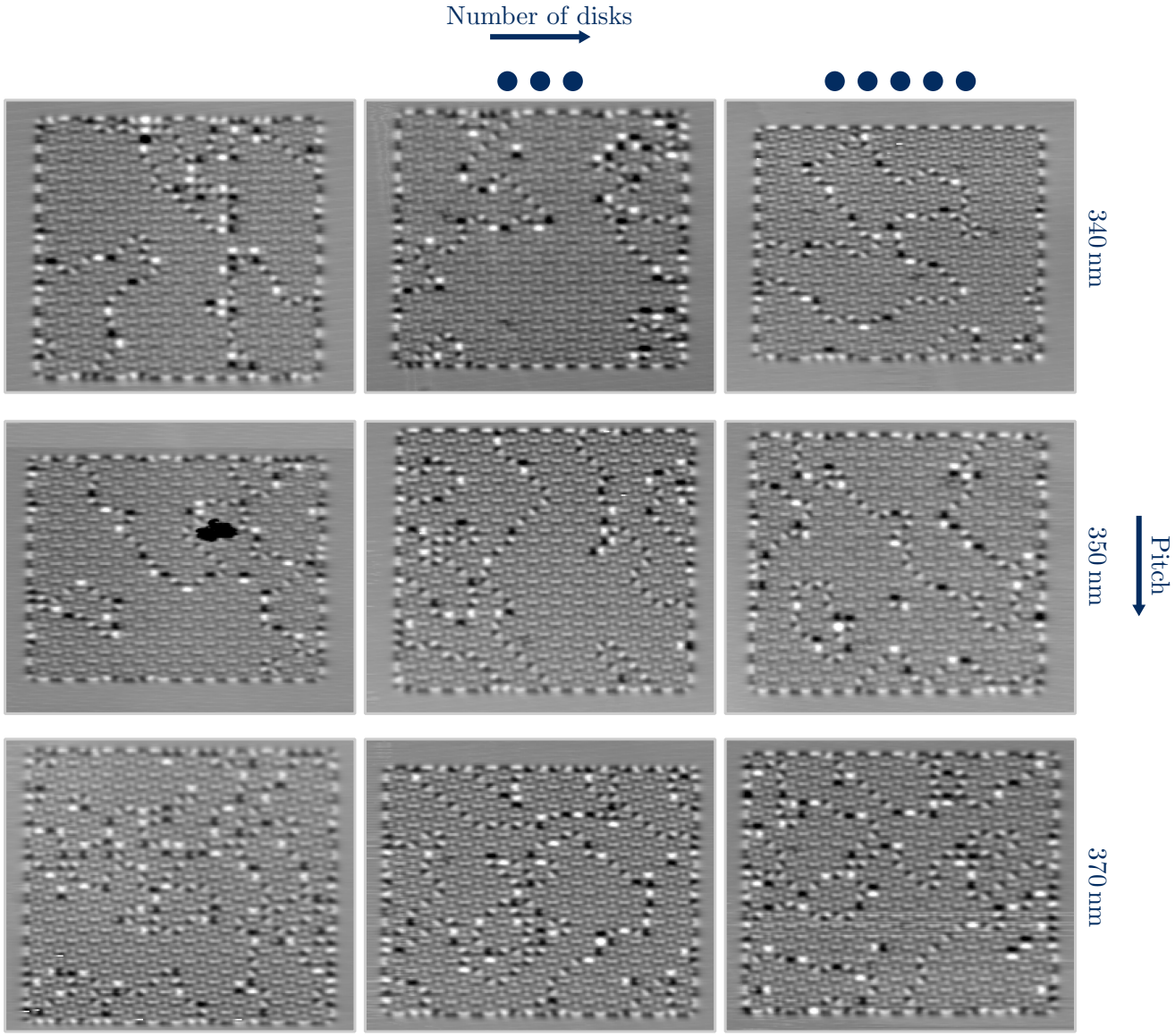

Figure 5.5: Nine different artificial spin ice ensembles with varying pitch and a varying number of added disks demonstrating ordered domains | The first column is standard square artificial spin ices, whereas the images in the second column contains three added disks, and the images in the third column contains five. The location of the added disks in the arrays are given in Fig. 4.4. The pitch of the arrays increases downwards. The peculiar black patch on the leftmost image in the middle row is caused by incomplete lift-off. One thing that can be noticed from the images is that there seems to be somewhat different shapes of the arrays, when we know that they should all be squares. The regular array with 350 nm-pitch appears elongated and rectangular for instance. This effect is caused by non-linearity in the piezoelectric actuators controlling the sample stage movement. The lift height is between 75 nm and 80 nm. The field of view is roughly 12.5 µm × 10.5 µm in all images.

thicknesses of the magnet islands, and arrange in the ground state during deposition, before they "freeze" in an arrangement as the thickness reaches a certain threshold. What we are imaging is then the frozen-in residue from the ordering that happened during fabrication.

The presence of the disk defects seemingly plays a minimal role in governing the as-grown magnetization state of the arrays. Comparing the three image columns does not reveal any different characteristics in the ensemble states with the presence of none, three or five disks. From our knowledge of the placement of the disk defects (Fig. 4.4), and by visual inspection of the images, the disk defects seem to be evenly distributed in the different ensemble features (ground state, strings and localized deviations). As such, there is no apparent trend indicating that the disks alter the ensemble state in its vicinity. The question is whether we expected there to be any. Our circular disk, with a diameter of 200 nm and thickness of 10 nm, is sufficiently large to favor a vortex state over a single domain one [47]. If the disks naturally take on a vortex state, then their stray field *in* the sample plane is minimal [48]. The vortex state of the disk does admittedly have a stray field. However, this is produced by what is called the vortex core, which is the midpoint of the flux closure. The vortex core has a magnetization pointing out of the plane, in either direction, and is in addition very small, typically about 10 nm [49]. The stray field produced from the vortex core will thus be perpendicular to the plane of the disk, and hence perpendicular to the nanomagnet moments. To alter the energy landscape for the elongated nanomagnets surrounding the disk, a magnetic field with a component *in-plane* is needed, as the Zeeman energy is zero if $\mathbf{H}$ and $\mathbf{M}$ are perpendicular (Eq. 2.3). If the disks naturally take on a vortex state, we might expect their influence on the neighbor magnets to be small. In which case, the arrays order like there had been no disk defects present at all.

If it is so that the presence of the disk is somewhat unnoticed in the array without the application of external fields, the next interesting question to pursue is how the presence of the disk defects potentially affect the switching in the array when an external field is applied, which is the topic of the next section.

5.3.2 A Field Trip Through Modified Artificial Spin Ices

This section presents and treats results on the artificial spin ices with embedded disk defects, and with applied magnetic fields. Simulated results are presented first, and briefly discussed. Thereafter, experimental results are given and discussed. The fabricated small arrays have the exact geometry as some of the simulated geometries. Additionally, the experimental procedure partly mimicked the simulation scheme. The retrieved experimental results are therefore discussed in light of their agreement with the simulated results. The field protocol and imaging of the small ensembles were carried out in an identical fashion twice, and the correspondence between the two series is therefore also treated. Finally, results from imaging the large arrays, after exposure to magnetic fields, are presented.

Simulations

The results of micromagnetic simulations are summarized in the plots in Fig. 5.6 and Fig. 5.7. The first figure (Fig. 5.6) shows how the presence of a disk with a varying diameter in the array alters the switching characteristics. Each plot belongs to one disk diameter, except for the top leftmost plot which correspond to an array without a disk. The regular array with no disk included has a narrow field range in which switching of the magnets take place, and almost every magnet in the array – comprising 60 in total – switch at the same field strength of 46 mT. In the case where a 60 nm-diameter disk is included, the effect is miniscule, and the plot is close to identical to the one with no disk. However, as the size of the disk increases, so does the effect it has on the switching characteristics. For increasing diameters of the disk, the

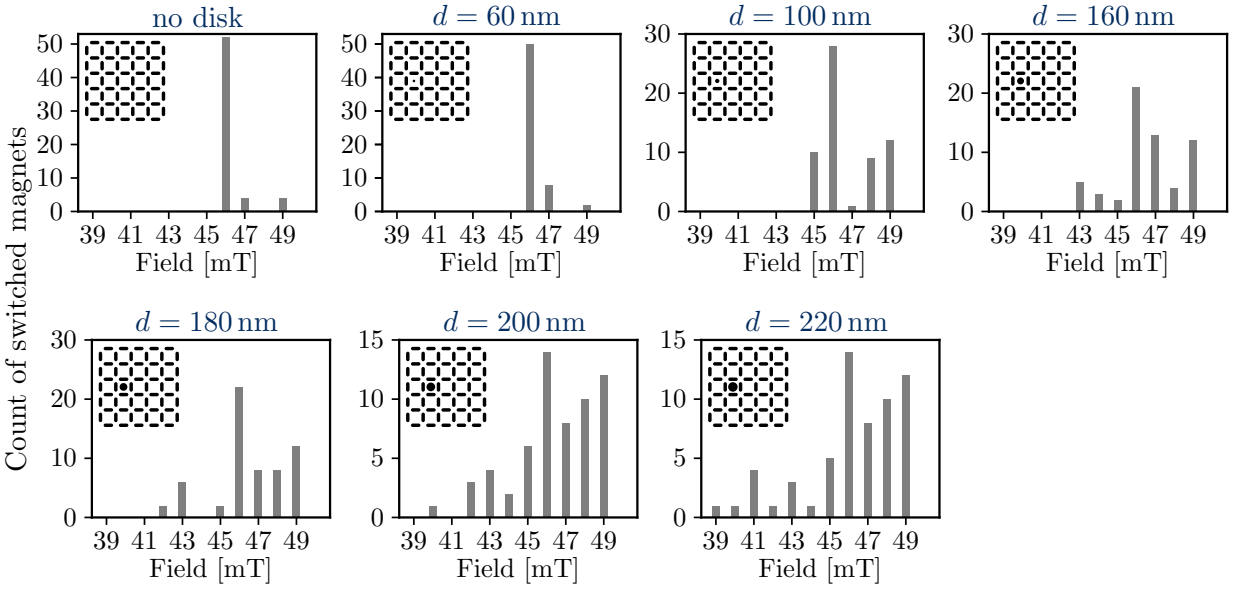

Figure 5.6: Simulated switching characteristics as a function of a varied diameter of the embedded disk | The plots present the number of switched magnets in the array at different magnetic field strengths. One plot belongs to one disk diameter, d, and the pitch of all the arrays is 350 nm. Inset in every plot is the simulation geometry. The vertical axis is the count of switched magnets. Notice how the values on the vertical axis are different between the plots to better fit the data. Summing the height of the bars in each plot should amount to 60 in total.

onset of the first magnetization reversals in the array is shifted to lower values of applied field, thus widening the field range in which reversals take place. For the 220 nm-diameter disk, the first reversals take place at 39 mT, corresponding to a field strength of 7 mT lower compared to the regular array. In all cases, every magnet in the array has reversed its magnetization at 49 mT.

The effect of varying the pitch of the array is shown in the plots in Fig. 5.7. Here the disk diameter is the same – 200 nm – in all the plots. Varying the pitch of the array also affects the switching characteristics. It is more challenging to spot a clear trend in the plots in Fig. 5.7, compared to what we saw in Fig. 5.6. However, what is evident, is that smaller pitches shift the onset of reversals in the array to lower values of the field. The first switching events take place at 38 mT in the 320 nm-pitch array, compared to at 42 mT for the 370 nm-pitch array.

The count of reversed magnets after each incrementation of the field (as presented in the bar plots) does not reveal all information about the switching process. To appreciate the difference between a regular array and one with a disk embedded, the location of the magnets that are switching should be given. The evolution of the magnetization state of the regular array, and one with an included 200 nm-diameter disk, upon applying increasing positive fields is given in Fig. 5.8a and Fig. 5.8b, respectively. Both arrays have a pitch of 350 nm. The regular array is in the initial polarized state with all the vertical magnets magnetized upwards and all the horizontal magnets magnetized towards the left until 46 mT. At 46 mT almost every magnet reverses its magnetization, as also seen in the bar plot (Fig. 5.6 and no disk). For the array with the embedded disk, the magnetization of the disk is uniform and aligns with the direction of the applied field. At 40 mT the first magnet in the array switches (the closest magnet to the right of the disk).

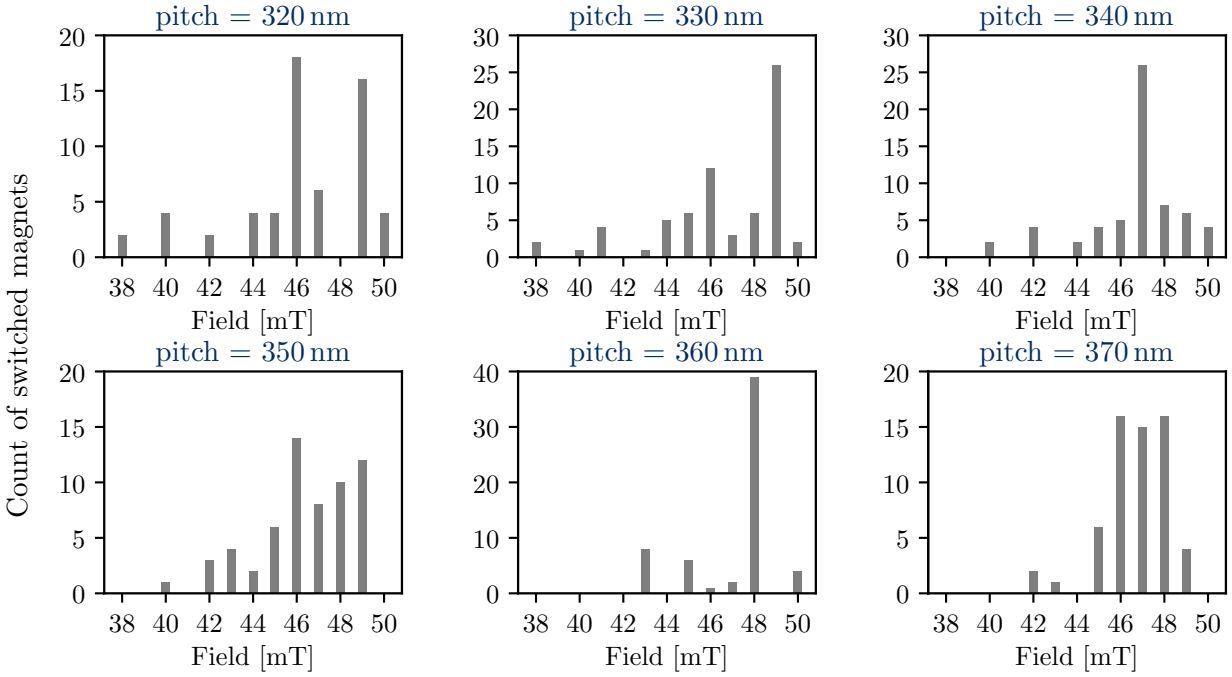

Figure 5.7: Simulated switching characteristics as a function of varying the pitch | All the simulation geometries have a 200 nm-diameter disk in the array, with the same placement as in the simulation geometry given in the previous figure (Fig. 5.6). The pitch of the arrays varies from 320 nm to 370 nm. The vertical axis presents the count of switched magnets, and the values on the vertical axis is different between some of the plots.

Following the initial switch, the evolution takes on an interesting appearance. The switching of the magnets follows a string that grows from the initial reversed magnet with the application of 42 mT and then 43 mT. After 45 mT the flipped magnets make up two adjacent strings with the disk in between. The magnetization state after application of 47 mT shows a high degree of ground state ordering. The switching evolution, with the neighboring magnets to the disk being the first to switch followed by this string growth, is representative for all the pitches and disk diameters simulated (except for the disk of 60 nm-diameter), with small alterations. However, the onset of the reversals depends on the geometry, as seen from the plots in Fig. 5.6 and Fig. 5.7.

From the simulated results, both the plots and the magnetization states, it is clear that the presence of a disk (with a sufficiently large diameter) alters the switching evolution from one polarized state to the opposite compared to a regular array. The switching nucleates from the magnets in the vicinity of the disk. The energy needed to switch the elongated nanomagnets is provided by a magnetic field through the Zeeman energy. For the magnets embedded in the array, the field experienced by a single magnet will not be composed solely of an externally applied field, but also of the dipolar fields created by the surrounding magnets. Upon introducing a disk, we add additional stray field – the stray field produced by the disk – which will act upon the nearby magnets. From the magnetization states (Fig. 5.8), the magnetization of the disk is uniform and in the direction of the field. These properties underscore the motivation for using the circular disk shape, in that it has no in-plane shape anisotropy. The barrier for magnetization reversal for the elongated magnets (Eq. 2.15) does not apply to the disk. From the simulations we see that the magnetization of the disk easily lines up with the axis of applied field. The disk can thus be said to act as a local enhancer of the field, as it takes on a uniform magnetization along the field direction and provides stray field. We do, on the other hand, know that the magnetic field is destined to circulate (Eq. 2.1), which imply that

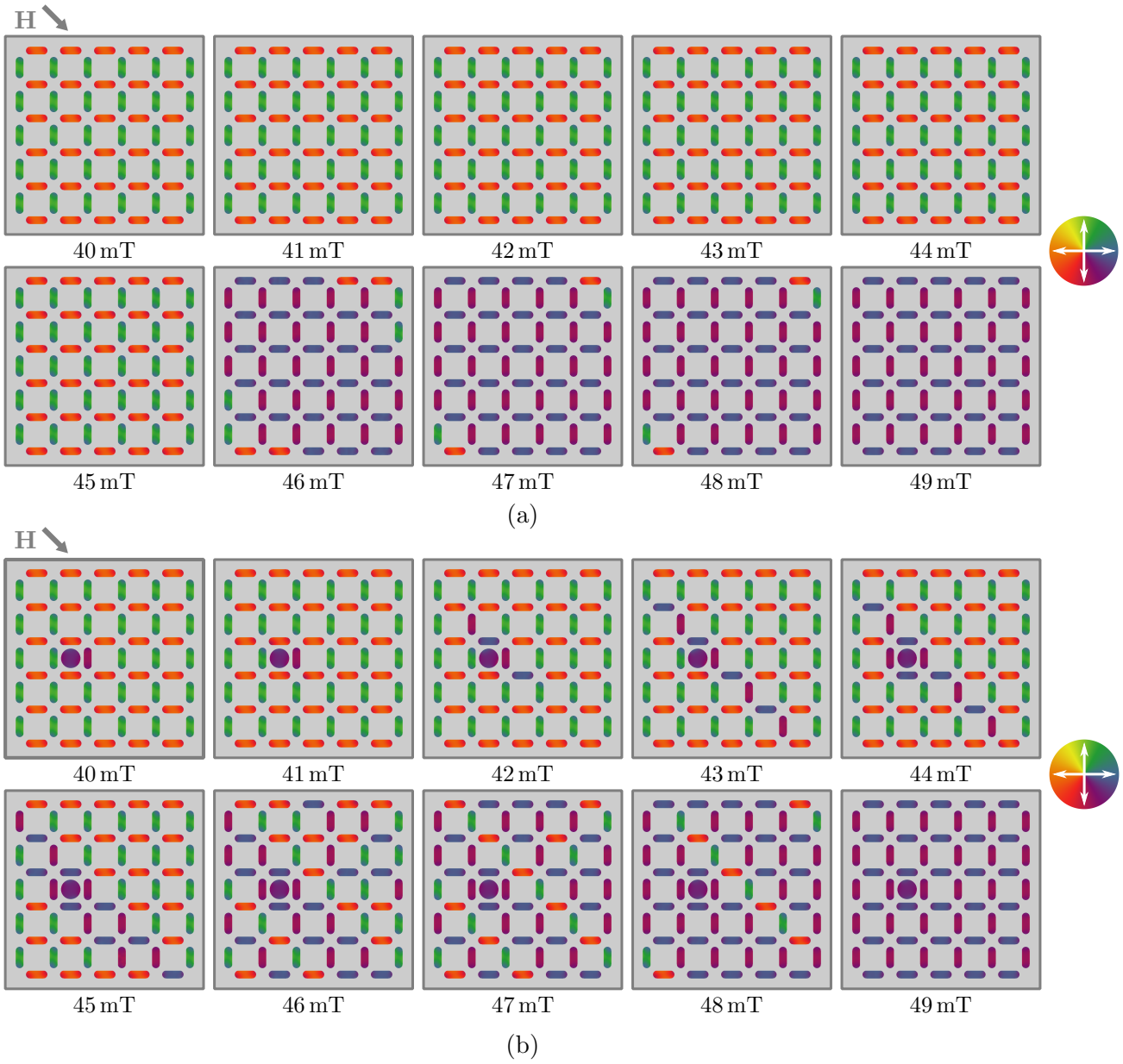

Figure 5.8: Magnetization states retrieved from simulations | **(a)** The simulation geometry is a regular array with a 350 nm pitch. The colormap indicates the connection between color and magnetization directions. The array was initialized in the saturated state with the vertical sublattice magnetized upwards and the horizontal sublattice magnetized towards left. No switches take place before application of 46 mT. **(b)** The pitch of the array is also here 350 nm. A disk with a 200 nm diameter is included in the simulation geometry. The array was initialized in the same manner as the regular array, and the disk was initialized with a uniform magnetization towards left. The first switching event takes place at 40 mT, with the right neighbor magnet to the disk. The switching sequence proceeds with a string-like growth until 46 mT.

the stray field from the disk also has components in the opposite direction to the applied field. Nonetheless, the simulation results show that the stray field produced from the disk acts on its nearest-neighbor magnets such that they are more prone to switching. Due to the coupling in the rest of the array, the first reversal sets off a string or avalanche growth of reversing moments.

With the disk acting as a field enhancer by virtue of its stray field, the trend with an earlier onset of magnetization reversals as the diameter increases is as expected. A larger disk diameter yields a large volume of magnetic material, and consequently a larger stray field. In varying the pitch (Fig. 5.7) there is a narrowing of the switching field window as the pitch increases. This is also what one would initially expect. Increasing the pitch increases the distance between the embedded disk and the surrounding magnets, and the interaction between the disk and surrounding magnets becomes weaker (Eq. 2.4, approximating both the disk and the neighbor magnets as point dipoles).

Experimental MFM images of the Small Ensembles

A selection of some of the experimentally retrieved MFM images of a 340 nm-pitch array and a 350 nm-pitch array comprising 60 magnets – like the simulated arrays – are presented in Fig. 5.9 and 5.10, respectively. In both arrays, a nominally 200 nm-diameter Py disk is located at the same position as in the simulation geometries. The first image row, in both figures, is the experimentally captured MFM images. The direction and values of the field that was applied, prior to reducing the field to zero and imaging, is as indicated in the figure. The second row are simulated images made using the MFM image generator in mumax3 and are included to verify the decoded states that are illustrated in the third image row. The placement of the disk is shown. The simulated MFM images are, however, made without a disk present in the array, and because we cannot be sure of the magnetization direction of the disk in the experimental case, the disk is colored gray.

In both arrays the first magnet(s) to switch belong to the group of the four magnets surrounding the disk. For the 340 nm-pitch array (Fig. 5.9) the ensemble is in the saturated state until 28 mT is applied, at which point the two vertical magnets next to the disk switch. It is not until the application of 35 mT that more switching events take place. At 36 mT, there are two patches of low contrast in the experimental (and simulated) MFM image, corresponding to ground state ordering. At 39 mT, only a few magnets have not switched. For the 350 nm-pitch array (Fig. 5.10) the first magnetization reversal takes place at 29 mT, with the vertical magnet to the right of the disk. Increasing the field leads to more switching events. Compared to the 340 nm-pitch array there is a smaller extent of ground state ordering during the reversal process.

Having resolved the exact experimental magnetization states, we can make plots of the spread in the switching window (the range of fields where switching occurs) and the number of magnets reversing their magnetization at each field value, to provide a direct analogy to the statistics retrieved from simulations. Such plots are given in Fig. 5.11a for the 340 nm-pitch array, and in Fig. 5.12a for the 350 nm-pitch array. The height of the bars is the number of switched magnets counted from the experimental images (or rather, counted from the experimental images translated to a magnetization state) after applying the corresponding field strength. Even though the geometry, the temperature and the field applied are the same in the two rounds, there are certain differences in the plots. Moreover, as with the bar plots belonging to the simulations, the plots in Fig. 5.11a and 5.12a neither tells the entire story (equally many magnets could have switched in the two series, but solely on different locations). Fig. 5.11b and 5.12b illustrates the differences in the magnetization states between the two series, the colored magnets highlight which magnets have switched differently.

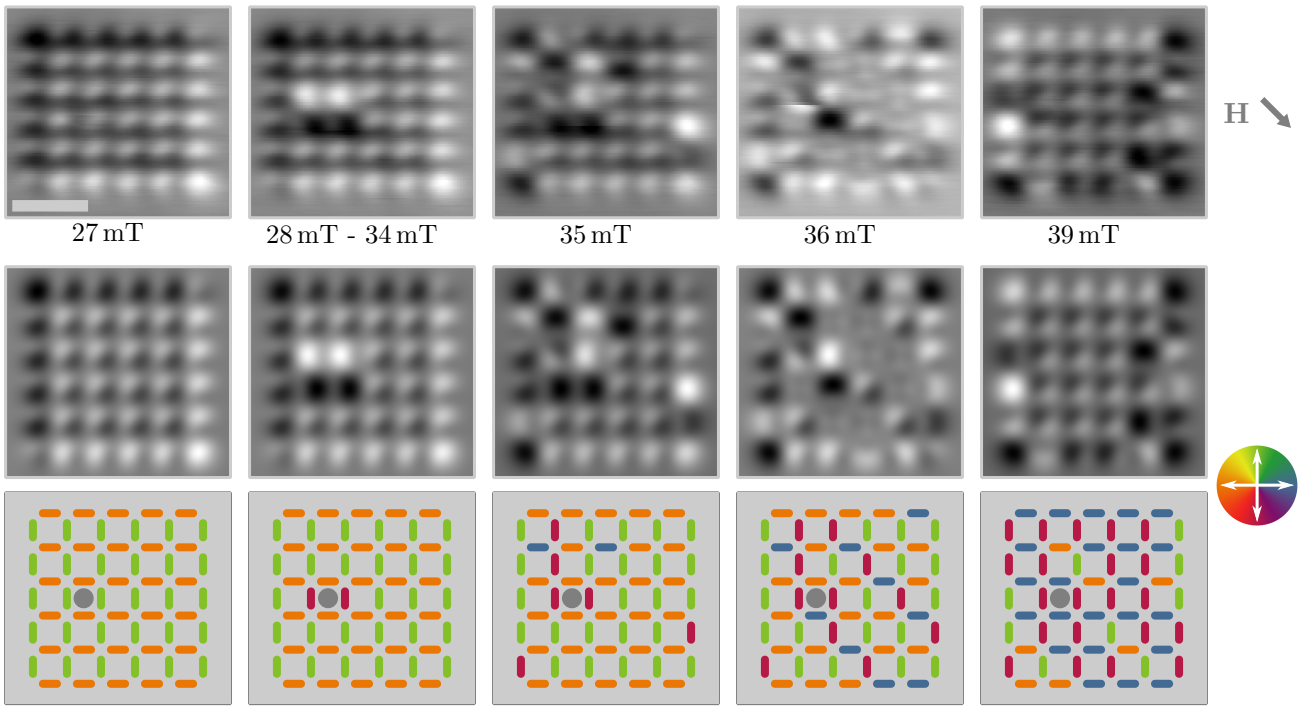

Figure 5.9: Experimental MFM images and the corresponding magnetization state of the small 340 nm-pitch array | The top row is experimentally retrieved MFM images of the fabricated 340 nm-pitch array with a 200 nm-diameter disk. The field values beneath the images correspond to the applied fields in the cryostat. The direction of applied field is shown. The lift height of the tip is 70 nm in all five images. The scale bar on the leftmost image is 1 µm, and the four images beside share the same dimensions. The second image row are simulated MFM images made from the magnetization states in the third row. The placement of the disk is shown in the magnetization state images. The simulated images are included as a verification of the mapping between the experimental image and the resolved state. Colormap included for reference.

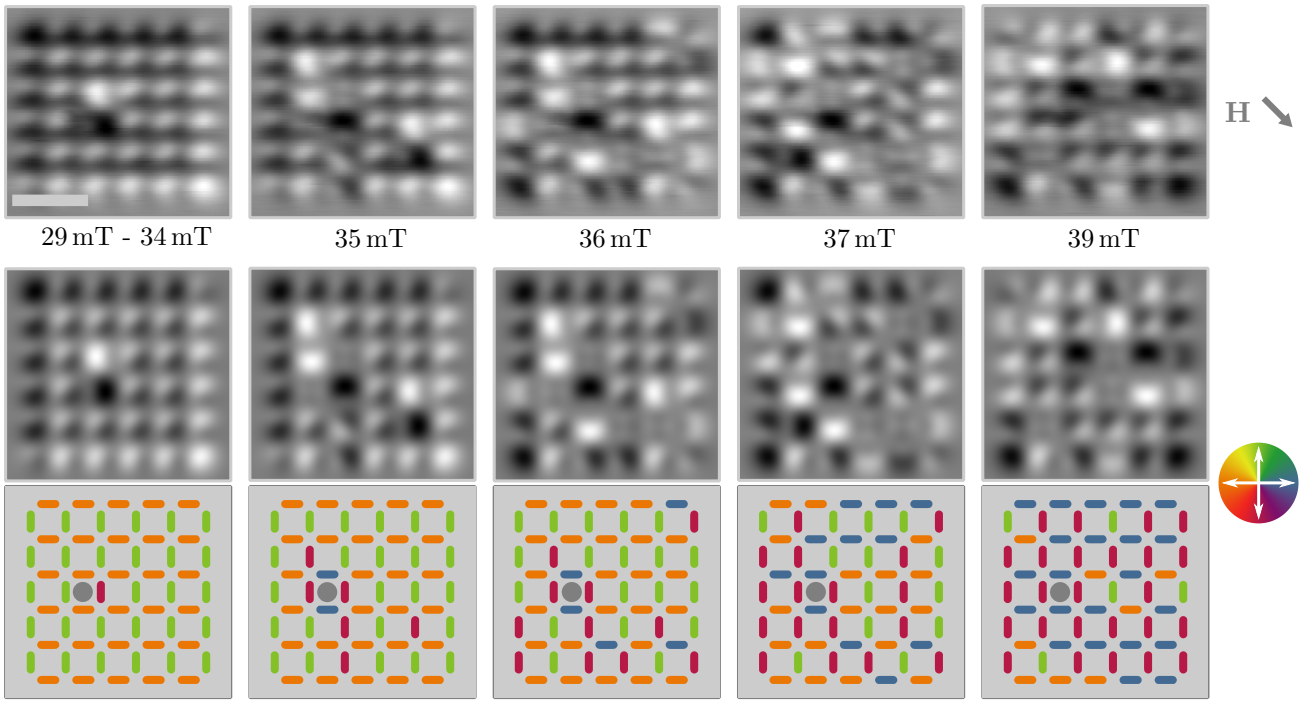

Figure 5.10: Experimental MFM images and the corresponding magnetization state of the small 350 nm-pitch array | The top row is experimentally retrieved MFM images of the fabricated 350 nm-pitch array with a 200 nm-diameter disk. The lift height of the tip is 75 nm in all five images. The scale bar on the leftmost image is 1 µm, and the four other experimental images share the same dimensions. The second image row are simulated MFM images made from the magnetization states in the third image row. Colormap included for reference.

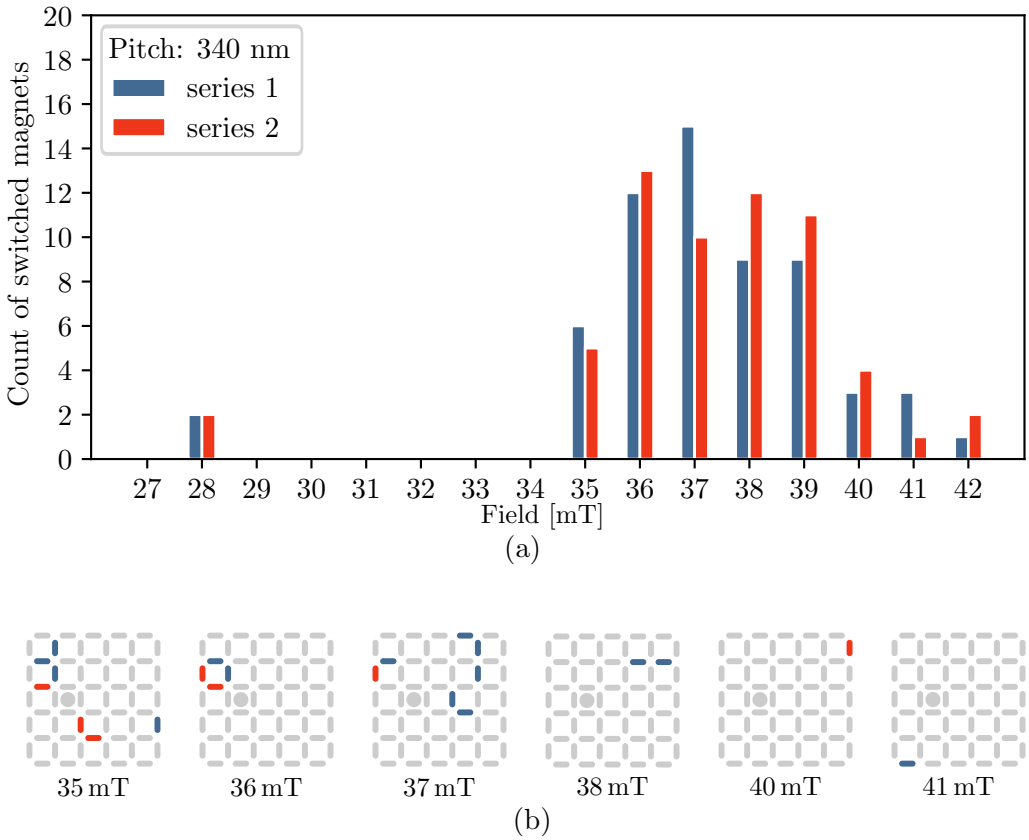

Figure 5.11: Experimental switching data for the 340 nm-pitch array | **(a)** The height of the bars gives the number of magnets that have switched at the given value of applied field. The blue bars correspond to the first round (the images in Fig. 5.9 are from series 1) of field incrementation and imaging, and the red bars correspond to the second round of repeating the same procedure. **(b)** These illustrations show the differences between the two series. The blue colored magnets correspond to magnets that have switched in series 1 and *not* in series 2 at the field value given beneath, whereas the red colored magnets are the ones that have switched in series 2 and not in series 1. The values of the field that is not represented with such an illustration of the array has an equal magnetization state in the two series. This is the case for the field values 28 mT to 34 mT, 39 mT and 42 mT.

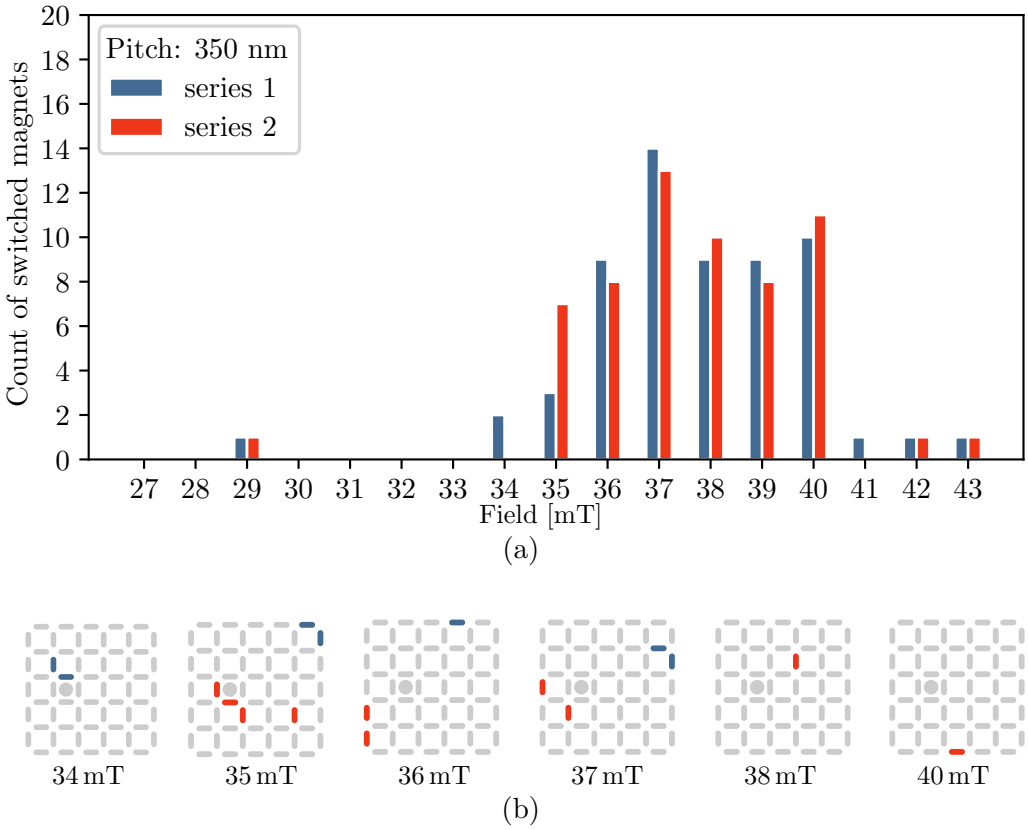

Figure 5.12: Experimental switching data for the 350 nm-pitch array | **(a)** The blue bars correspond to the first image series and the red ones to the second series (the images in Fig. 5.10 are taken from the second series). **(b)** The blue colored magnets correspond to magnets that have switched in series 1 and not in series 2 at the field value given beneath, and the red colored magnets are the ones that have switched in series 2 and not in series 1.

Similar to in the simulations, the presence of the embedded disk in the small arrays does not go unnoticed upon application of magnetic fields. In Fig. 5.9 and 5.10, neighboring magnets to the disk reverse their magnetization first, and they do so at substantially lower fields compared to the field at which other magnets in the array switch. The two vertical magnets next to the disk in the 340 nm-pitch array switches at 28 mT, and it is not until 35 mT that more switching events take place. In both the 340 nm-pitch and 350 nm-pitch arrays, one could say that the reversals that follow up, after application of 35 mT, nucleates from the first reversals. However, three magnets in the 340 nm-pitch array are not connected to the "string" from the disk, and in the 350 nm-pitch array one lone magnet unconnected to the rest has switched. Although the disk modifies the switching in the physical arrays, by initializing reversals of its neighbor magnets, none of the evolutions (i.e., which magnets reverse at which field strength) mimics exactly the evolution seen in simulations.

Certain discrepancies between simulated and experimental results are not unheard-of. There are several sources that may contribute to the observed differences here, considering that some traits of the real world are not taken into consideration in the simulations. The perhaps most defining feature of the experimental array as opposed to the simulated one, is the presence of the quenched disorder. In simulations, every magnet is identical, but we know from the previous section (Section 5.2), that this is not the case for the fabricated magnets. The switching evolution of a physical array can thus be expected to deviate from a simulated one, as there simply are magnets with different properties (switching field) compared to in simulation. Additionally, in the experimental case we are imaging with a tip that has associated stray field and affect the experienced field for the single magnets to some degree. Moreover, there was a finite temperature of 8 K during the acquisition of all the experimental images, while temperature is not included in the simulations. Temperature contributes with some randomness in the switching, as the thermal energy might assist in the leap over the switching barrier for the nanomagnets (Section 2.3.1).

Furthermore, in simulations we have full control on the value, the direction, and the duration of the applied magnetic field, while in the experimental case we do not have that to the same degree. The electromagnet has a limited resolution on the field it provides. Additionally, as the electromagnet ramps up its field by increasing the current there is a probability for overshooting the current, and consequently the field created. Moreover, the duration of applied field is hard to control experimentally as the sample is exposed to the field from the electromagnet while it ramps up and down. Finally, despite our efforts in Section 5.1, we cannot be entirely sure of the direction of the field. The Py rings and single nanomagnets were placed on one and the same sample, whereas the artificial spin ices with the embedded disk(s) were fabricated on a second sample. The microscope was for both samples rotated approximately 15° clockwise, but the two 15° rotations might be a little bit different.

Comparing the bar plots in Fig. 5.11 and 5.12, with the corresponding ones retrieved from simulations in Fig. 5.7, there is a notable difference in the field values on the abscissas. The switching occurs at considerably lower values of the applied field in the physical array, compared to in simulations. Moreover, the first bars in the experimental plots are more separated from the rest, compared to in the simulation plots. As was pointed out in Section 2.3.1, edge roughness will often act to decrease the coercive field. Therefore, we can expect the mean switching field of the physical magnets to be lower than what simulations of the same (but perfect) geometry would have us believe. This also seems to be the case. The histogram plot in Fig. 5.3 yielded an expectation value for the coercive field (with a field 45° to the long axis of the magnets) of 46 mT, while micromagnetic simulations of a single magnet in mumax3 reveals a coercive field of 48 mT, which is somewhat higher. The difference between the simulated and measured coercive

field is still perhaps not large enough to explain the different field values on the abscissas.

Beyond a lower coercive field of the magnets in the physical array compared to the simulated one, a weaker coupling between the magnets could also provide an explanation for the lower perceived fields. The first magnets to switch in the arrays do so by changing two type II vertices into two type III vertices. A weaker coupling yields a smaller energy difference between the two vertices, thus lowering the barrier for the first magnets to switch. The large separation between the first and the following bars in the experimental switching data support this suggestion. In the simulated state evolution in Fig. 5.8b the first reversal adjacent to the disk is followed up by a string of reversals after increasing the field with 2 mT. The string growth is a consequence of the coupling, because the first magnet that switches creates two unfavorable type III vertices, which are converted to type I vertices by continued string growth. Seeing as, in the experimental case, there is a larger separation in field from the first to the following reversals, it might tell a story of a weaker coupling.

In addition to differences between the simulated and the experimental evolutions, the switching evolution for the fabricated small ensembles varies when applying the same field protocol twice, i.e., the manner of switching is not entirely reproduced. In Fig. 5.11b and 5.12b, the differences between the two series are highlighted. The maximum number of deviations is found after application of 35 mT and 37 mT to the 340 nm-pitch array (Fig. 5.11b), where in both cases seven magnets have switched differently. For the 350 nm-pitch array (Fig. 5.12b) and at all other field strengths for the 340 nm-pitch array the number of deviations is less. These discrepancies must be understood as arising from some of the sources mentioned prior, that is, randomness introduced by the presence of a finite temperature, as well as differences in the field, in terms of duration and possibly overshooting. By virtue of the coupling in the array, it is also the case that once one or several magnets have switched differently between the two series, the energy landscape is altered. When subsequent fields are applied, the "starting conditions" are different, and hence, the field might induce different switches. In this regard, we can perhaps not blame quenched disorder (we are imaging the exact same physical array), or the direction of the field for the observed differences, as these parameters will stay the same. Despite some deviations in the evolution of the switching, the first switches that take place adjacent to the disk happens at the same field in both series, for both arrays.

Experimental MFM images of the Large Ensembles

Large artificial spin ice ensembles with five added disks defects, after being saturated to one polarized state and subsequently exposed to an increasing field in the opposite direction is given in Fig. 5.13. Images of a 340 nm-pitch ensemble are given in Fig. 5.13a, Fig. 5.13b are images of a 350 nm-pitch ensemble, and Fig. 5.13c are images of a 370 nm-pitch ensemble. In both the 340 nm-pitch array and the 350 nm-pitch array the disk locations are easily recognized in the images at 30 mT. The 340 nm-pitch array (Fig. 5.13a) has the first switching events at 30 mT. Until the application of 33 mT, only magnets localized around the disks have switched, but at 33 mT one horizontal magnet unrelated to the disks switches. For the 350 nm-pitch array, the first reversals also take place at 30 mT. However, already at the application of 31 mT, equally many magnets located around the disks and elsewhere in the array has switched. For the 370 nm-pitch array, the switching is more frequent in random locations than around the disks at 30 mT.

It is interesting to ask whether we would expect the transition from a small array to a large(r) to make much of a difference. One thing that is observed, when comparing the large 340 nm- and 350 nm-pitch arrays with the small ones (Fig. 5.11a and Fig. 5.12a) is that the onset of reversals is shifted to slightly higher fields, the difference is 2 mT for the 340 nm-pitch array

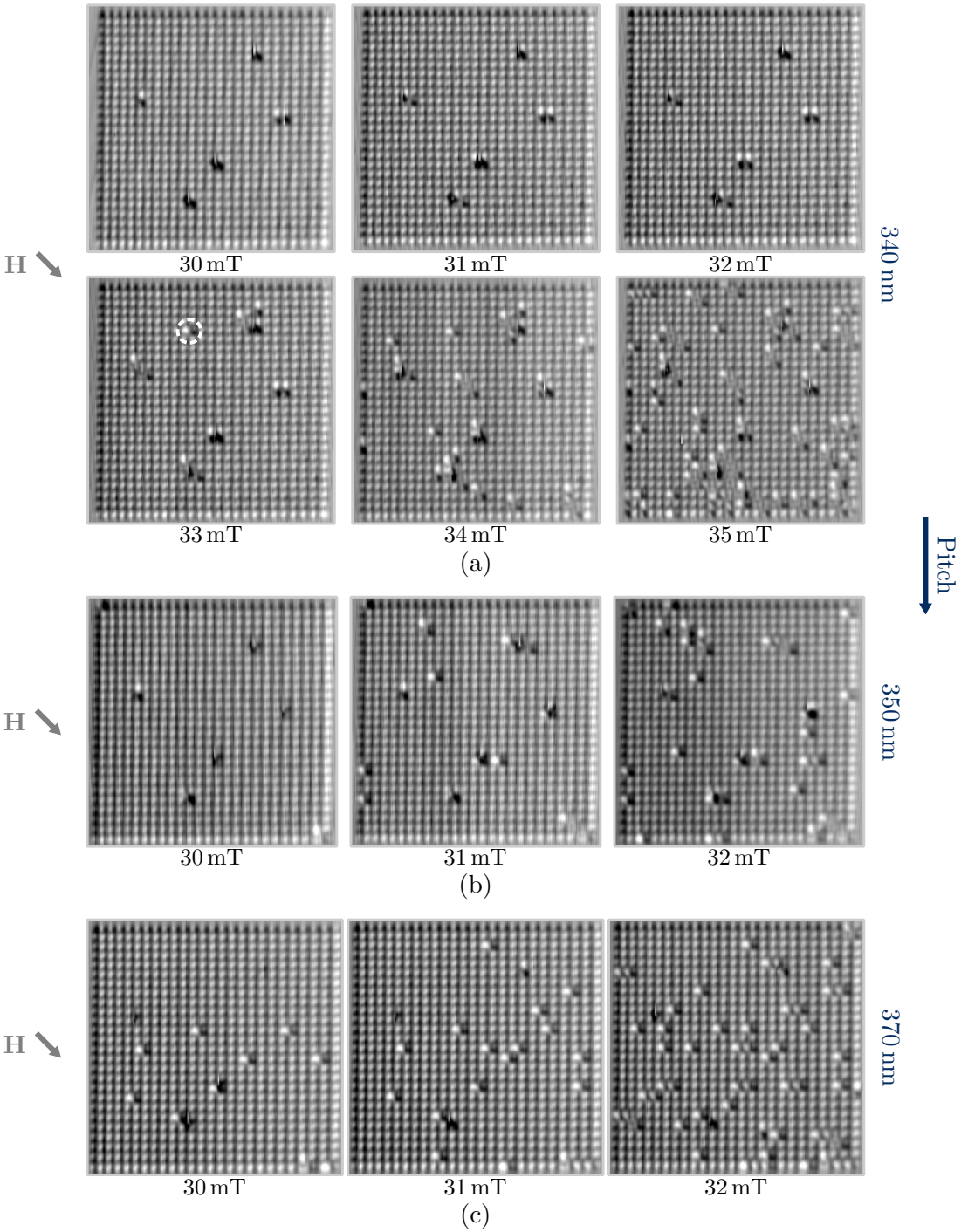

Figure 5.13: Switching of the large artificial spin ice ensembles with five added disks | **(a)** A 340 nm array. The locations of the disks are recognized by the prominent features in the array at 30 mT. After 32 mT the switching events that have taken place are all tied to the disk locations, whereas at 33 mT one horizontal magnet has switched unrelated to the disk, marked with a circle. After 34 mT we both have reversals that have spread from the disks, but also quite a few instances of switching events in the remainder of the array. The tip lift height is 70 nm to 75 nm. The field of view is approximately 10.5 µm × 10.5 µm. **(b)** A 350 nm-pitch array. At 30 mT the two first switching events have occurred, with one vertical neighbor magnet to the leftmost disk as well as one in the lower right corner. At 31 mT switching has occurred around all the disks, but also in an equal extent elsewhere in the array. The tip lift height is 90 nm. The field of view is approximately 10.6 µm × 10.6 µm. **(c)** A 370 nm-pitch array. Here, at 30 mT quite a few magnets have switched, and the majority are not tied to the locations around the disks. The tip lift height is 75 nm. The field of view is roughly 11.2 µm × 11.2 µm.

and 1 mT for the 350 nm-pitch array. In addition, the reversal of other magnets in random locations happens at lower fields in the large arrays. These two effects combined makes the disk effectively "less pronounced". Because we are only comparing one instance of a fabricated large array with one small array (for both pitches, 340 nm, and 350 nm), our data is too scarce to conclude on whether the effect of higher fields needed to switch the magnets around the disks can be attributed to the increased number of magnets. A probable explanation is that it is a consequence of random fabrication differences. If the disks in the small arrays happen to be slightly larger than in the large arrays, or if the surrounding magnets happen to be among the magnets with lower switching field, then one, or both, of these factors could give the perceived earlier onset in the small arrays. If, however, the effect is a consequence of the increased number of magnets, one could imagine the individual magnets in the large arrays to be slightly more "bound". In the large array there are considerably more magnets contributing with their dipolar fields, which might make the onset for switching somewhat higher in this case. However, the dipolar interaction energy falls off with r^3, and the dominant interaction in the lattices is therefore between the neighbor magnets. The prior emergence of "random" switches in the large arrays is, however, perhaps not very surprising. In the large array, there will be a larger population of early (and late) switchers, as there simply are more magnets.

Comparing the different pitches, there are mainly two aspects that are different. Firstly, in the 340 nm-pitch array the effect of the disk is markedly larger than in the two other arrays. A smaller pitch increases the interaction between the disk and the surrounding magnets. This effect is shown quite clearly from the images, and also agree with simulation results. Another trait to note is how the number of switched magnets at comparable field strengths increases with increased pitch. The 370 nm-pitch array has "gotten much further" than the 340 nm after 32 mT, for instance. The explanation lies once again in the coupling of the magnets. Because of the dipolar coupling, the difference in energy between a type II and a type III vertex is smaller for an array with a large pitch. As mentioned earlier, the first switching events take place with a transition between the two. The barrier for switching is thus lowered in the arrays with larger pitches. This is a good example of how tuning the geometry gives different properties, even if the relevant parameter that is changed is only altered with some tens of nanometers.

It is hard to draw any conclusions on the magnetization state of the disk at remanence from the presented images. The imaged arrays in Fig. 5.13 are of the same type as those in Fig. 5.5, albeit with a very different appearance. Moreover, the disks are distinctly more visible in the images in Fig. 5.13a and b, as compared to almost invisible in the domain-images. In the image of the 350 nm-pitch array after 30 mT, the three rightmost disks are easily seen from the black contrast, which is not caused by any reversals of the array magnets. This might give cause to believe that the vortex state of the disk that was hypothesized in Fig. 5.5 was indeed the disk's magnetization state in the as-grown magnetization of the ensembles. One might expect the vortex state of the disk to be less pronounced in the MFM images because of the stray field from this magnetization state (however vertical) is created by the very tiny core. The reason why they are much more visible after application of field might then be explained by the disks having adopted a more uniform magnetization, like they do in the simulations (Fig. 5.8). The uniform magnetization of the disk would, however, be expected to have one end with white and one end with black contrast, like the elongated magnets, and this is not observed. There is seemingly only black contrast, which also seem to be somewhat smeared out. The best explanation for this is an interaction between the tip and the disk magnetization as the tip scans over the sample. The magnetization of the disk might rotate and temporarily align with the tip, which would make the interaction only attractive, and give solely black contrast.

Chapter 6

Conclusion

In this project work, studies of three different systems of nanoscale magnetic structures – rings, single nanomagnets, and square artificial spin ices with one or more incorporated disk defects – has been carried out. The main aim was to study the effect of adding a disk defect in the square artificial spin ice, and thus the investigation of the latter system has been given the most emphasis. The study of the two other systems has, however, provided us with valuable results and insights.

The direction of the field on the sample stage was successfully determined by applying a field to a thin film ring of Py and inducing an onion state symmetric about the axis of applied field. From the onion state, the direction of the field on the sample plane could be determined. For studying the two other systems in the MFM, this was a critical parameter to know. The finding will undoubtedly also be useful for successors in operating the instrument.

The spread in switching field for single nanomagnets, with a field applied at 45° to their long axis, was quantified. An array comprising single magnets with a separation of 1 µm, to make them non-interacting, were exposed to increasing values of an applied field, and imaged between each field incrementation. The images were then used to count the number of switched magnets in the array at each field value. Curve fitting a normal distribution to the experimental data gave a standard deviation in the switching field of 1.8 mT relative to a mean of 46 mT, at 8 K. These values yield insight to compare simulated and experimental results. It is also a result that can be used to improve upon simulations of artificial spin ice arrays by including this experimentally determined variation in the magnet properties into simulations.

Micromagnetic simulations of a square artificial spin ice with varying diameters of the added disk, and varying pitches of the lattice were carried out. With disks having a diameter above 100 nm, the application of magnetic fields led to the neighboring magnets to the disk reversing their magnetization first and setting of an avalanche of reversals. Some of the geometries investigated in simulations were fabricated and imaged in the MFM. The as-grown magnetization state of large arrays displayed domains of ground state ordering separated by Dirac Strings. There was no apparent trend in the images indicating that the presence of a disk had any prominent effects on these magnetization states. The switching characteristics with applied fields, however, revealed the disk to act as a nucleator for the neighboring magnets similar to in the simulated case. The following switching evolution in the experimental case does not proceed in the same manner, which among other factors is attributed to the presence of quenched disorder in the fabricated sample. In the experimental case the exact same field protocol was repeated twice and revealed that the magnets surrounding the disk switched reproducibly, however, the entire switching process was not reproduced.

Further Work

Retrieving more switching statistics on the non-interacting single nanomagnets that are the building blocks of artificial spin ices could be worthwhile. Here the switching distribution was quantified by applying a field at 45° to the long axis of the magnets and with a temperature of 8 K. Repeating the measurements at varying directions of applied field and varying temperatures could be valuable, both to gain a better understanding of the fabricated artificial spin ices and the role and extent of disorder, and to improve modelling of the systems.

In regard to the direction of applied field, this is also one parameter that could be altered in the study of the artificial spin ices with embedded disk defects. The disk with its circular shape is expected to respond similarly to fields applied at different directions, but the switching characteristics of the elongated magnets, however, depend upon the angle of applied field. Changing the direction of applied field in simulations is straightforward and can also be achieved experimentally by rotation of the microscope (and if one wants to verify the angle of the applied field, one could always fabricate a ring structure on the same sample).

If the inclusion of a disk is to be used as means for controlling the switching route, then reproducibility is a wanted trait. In this study, two rounds of the same field protocol were repeated and the switching sequence was not reproduced. To gain better understanding of the reproducibility of the systems several repetitions are needed. It is also interesting to investigate if the presence of the disks make the switching evolution more reproducible than in the case of a regular array.

Bibliography

[1] Nicola Jones. "How to stop data centres from gobbling up the world's electricity". In: *Nature* 561.7722 (2018), pp. 163–167.

[2] Mark Bohr. "A 30 year retrospective on Dennard's MOSFET scaling paper". In: *IEEE Solid-State Circuits Society Newsletter* 12.1 (2007), pp. 11–13.

[3] SA Wolf et al. "Spintronics: a spin-based electronics vision for the future". In: *science* 294.5546 (2001), pp. 1488–1495.

[4] Daniel C Mattis. *The theory of magnetism I: Statics and Dynamics*. Vol. 17. Springer Science & Business Media, 2012.

[5] Rainer Waser et al. *Nanoelectronics and information technology*. Wiley Online Library, 2012.

[6] Claude Chappert, Albert Fert, and Frédéric Nguyen Van Dau. "The emergence of spin electronics in data storage". In: *Nanoscience And Technology: A Collection of Reviews from Nature Journals*. World Scientific, 2010, pp. 147–157.

[7] Jack C Gartside et al. "Realization of ground state in artificial kagome spin ice via topological defect-driven magnetic writing". In: *Nature nanotechnology* 13.1 (2018), pp. 53–58.

[8] RF Wang et al. "Artificial 'spin ice' in a geometrically frustrated lattice of nanoscale ferromagnetic islands". In: *Nature* 439.7074 (2006), pp. 303–306.

[9] R Siddharthan et al. "Ising pyrochlore magnets: Low-temperature properties,"ice rules," and beyond". In: *Physical review letters* 83.9 (1999), p. 1854.

[10] Mark J Harris et al. "Geometrical frustration in the ferromagnetic pyrochlore Ho 2 Ti 2 O 7". In: *Physical Review Letters* 79.13 (1997), p. 2554.

[11] Sandra H Skjærvø et al. "Advances in artificial spin ice". In: *Nature Reviews Physics* (2019), pp. 1–16.

[12] Hanu Arava et al. "Engineering relaxation pathways in building blocks of artificial spin ice for computation". In: *Physical Review Applied* 11.5 (2019), p. 054086.

[13] Johannes H. Jensen, Erik Folven, and Gunnar Tufte. "Computation in artificial spin ice". In: *Artificial Life Conference Proceedings* 30 (2018), pp. 15–22.

[14] Laura J Heyderman and Robert L Stamps. "Artificial ferroic systems: novel functionality from structure, interactions and dynamics". In: *Journal of Physics: Condensed Matter* 25.36 (2013), p. 363201.

[15] Elena Mengotti et al. "Real-space observation of emergent magnetic monopoles and associated Dirac strings in artificial kagome spin ice". In: *Nature Physics* 7.1 (2011), pp. 68–74.

[16] Yong-Lei Wang et al. "Rewritable artificial magnetic charge ice". In: *Science* 352.6288 (2016), pp. 962–966.

[17] John MD Coey. *Magnetism and magnetic materials*. Cambridge university press, 2010.

[18] Nicola A Spaldin. *Magnetic materials: fundamentals and applications*. Cambridge University Press, 2010.

[19] É Du Trémolet de Lacheisserie, D Gignoux, and M Schlenker. *Magnetism*. Springer New York, 2002. ISBN: 9780387230627.

[20] Mathias Getzlaff. *Fundamentals of magnetism*. Springer Science & Business Media, 2007.

[21] Charles Kittel. *Introduction to Solid State Physics*. John Wiley & Sons, 2005.

[22] Michael P Marder. *Condensed matter physics*. John Wiley & Sons, 2010.

[23] David Jiles. *Introduction to magnetism and magnetic materials*. CRC press, 1991.

[24] Amikam Aharoni et al. *Introduction to the Theory of Ferromagnetism*. Vol. 109. Clarendon Press, 2000.

[25] C Tannous and J Gieraltowski. "The Stoner–Wohlfarth model of ferromagnetism". In: *European journal of physics* 29.3 (2008), p. 475.

[26] Yi Liu, David Sellmyer, and Daisuke Shindo. *Handbook of Advanced Magnetic Materials*. Jan. 2006.

[27] Thomas L Gilbert. "A phenomenological theory of damping in ferromagnetic materials". In: *IEEE transactions on magnetics* 40.6 (2004), pp. 3443–3449.

[28] Ralph Skomski et al. *Simple models of magnetism*. Oxford University Press on Demand, 2008.

[29] Roderich Moessner and Arthur P Ramirez. "Geometrical frustration". In: *Phys. Today* 59.2 (2006), p. 24.

[30] Joseph Sklenar, Sergi Lendinez, and M Benjamin Jungfleisch. "Dynamics in artificial spin ice and magnetic metamaterials". In: *Solid State Physics*. Vol. 70. Elsevier, 2019, pp. 171–235.

[31] Anders Strømberg. "Micromagnetic modelling and magnetic force microscopy of supermagnetism in patterned nanomagnetic arrays". Master's Thesis. Norwegian University of Science and Technology, 2018.

[32] Helmut Kronmüller and Manfred Fähnle. *Micromagnetism and the microstructure of ferromagnetic solids*. Cambridge university press, 2003.

[33] Alex Robinson and Richard Lawson. *Materials and Processes for Next Generation Lithography*. Elsevier, 2016.

[34] Beomseop Lee et al. "Sub-10-nm-resolution electron-beam lithography toward very-high-density multilevel 3D nano-magnetic information devices". In: *Journal of Nanoparticle Research* 15.6 (May 2013), p. 1665. ISSN: 1572-896X.

[35] O Kazakova et al. "Frontiers of magnetic force microscopy". In: *Journal of Applied Physics* 125.6 (2019), p. 060901.

[36] Daniele Passeri et al. "Magnetic force microscopy". In: *Magnetic characterization techniques for nanomaterials*. Springer, 2017, pp. 209–259.

[37] "Magnetic force microscopy". In: *Modern Techniques for Characterizing Magnetic Materials*. Ed. by Yimei Zhu. Boston, MA: Springer US, 2005, pp. 411–451. ISBN: 978-0-387-23395-6.

[38] Yurii P Ivanov and O Chubykalo-Fesenko. "Micromagnetic simulations of cylindrical magnetic nanowires". In: *Magnetic Nano-and Microwires*. Elsevier, 2015, pp. 423–448.

[39] J Rothman et al. "Observation of a bi-domain state and nucleation free switching in mesoscopic ring magnets". In: *Physical Review Letters* 86.6 (2001), p. 1098.

[40] Sam Ladak et al. “Direct observation of magnetic monopole defects in an artificial spin-ice system”. In: *Nature Physics* 6.5 (2010), pp. 359–363.

[41] Stephen A Daunheimer et al. “Reducing disorder in artificial kagome ice”. In: *Physical review letters* 107.16 (2011), p. 167201.

[42] SD Pollard, V Volkov, and Y Zhu. “Propagation of magnetic charge monopoles and Dirac flux strings in an artificial spin-ice lattice”. In: *Physical Review B* 85.18 (2012), p. 180402.

[43] KK Kohli et al. “Magneto-optical Kerr effect studies of square artificial spin ice”. In: *Physical Review B* 84.18 (2011), p. 180412.

[44] Zoe Budrikis, Paolo Politi, and RL Stamps. “Disorder regimes and equivalence of disorder types in artificial spin ice”. In: *Journal of Applied Physics* 111.7 (2012), 07E109.

[45] Jason P Morgan et al. “Thermal ground-state ordering and elementary excitations in artificial magnetic square ice”. In: *Nature Physics* 7.1 (2011), pp. 75–79.

[46] Sheng Zhang et al. “Crystallites of magnetic charges in artificial spin ice”. In: *Nature* 500.7464 (2013), pp. 553–557.

[47] Russell P Cowburn et al. “Single-domain circular nanomagnets”. In: *Physical Review Letters* 83.5 (1999), p. 1042.

[48] M Kläui et al. “Vortex formation in narrow ferromagnetic rings”. In: *Journal of Physics: Condensed Matter* 15.21 (2003), R985.

[49] L Rondin et al. “Stray-field imaging of magnetic vortices with a single diamond spin”. In: *Nature communications* 4.1 (2013), pp. 1–5.

Appendices

Appendix A

The Microscope and the Direction of Applied Field

The figure below provides an illustration of the cryostat chamber, and of the microscope and the field direction. The leftmost illustration shows the microscope in its standard position. The right illustration shows the microscope rotated 15° clockwise from its standard position, in which case the direction of applied field is at 45° counterclockwise from the vertical sample axis, as illustrated. The schematic of the microscope is adapted from an Attocube manual. The details of the illustrations are included for future users in operating the microscope.

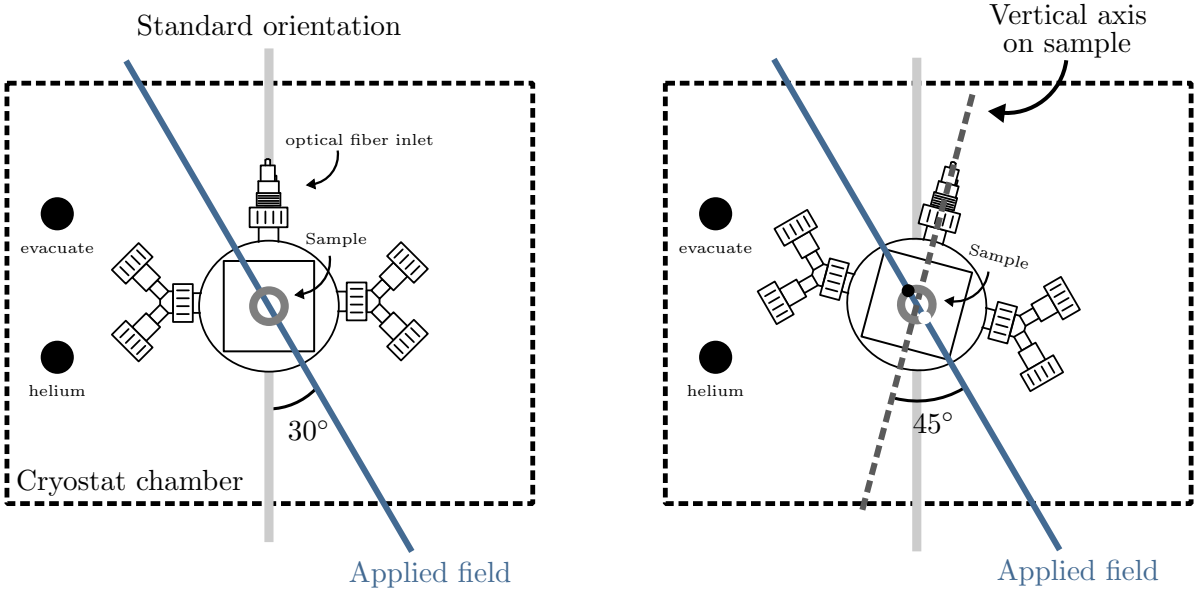

Appendix B

Counting the Switching Events for the Single Nanomagnets

The included images are one full image series captured to quantify the spread in switching field. The field of view in all the images is approximately 21 µm × 21 µm. The field values above each image correspond to the field strength the array was subjected to, before the field was lowered to zero and the image was captured. The third image column are images made by subtracting the MFM images of the second image column with those in the first. By doing this, the magnets that have their magnetization in opposite directions becomes clearly visible, and makes the counting easier. The features on the subtracted images can be counted manually, but particle recognition functionality in ImageJ was found to work very well. It should be noted that only half of the subtracted images belonging to the presented series is given, for instance the difference between 41 mT and 40 mT is not shown here.

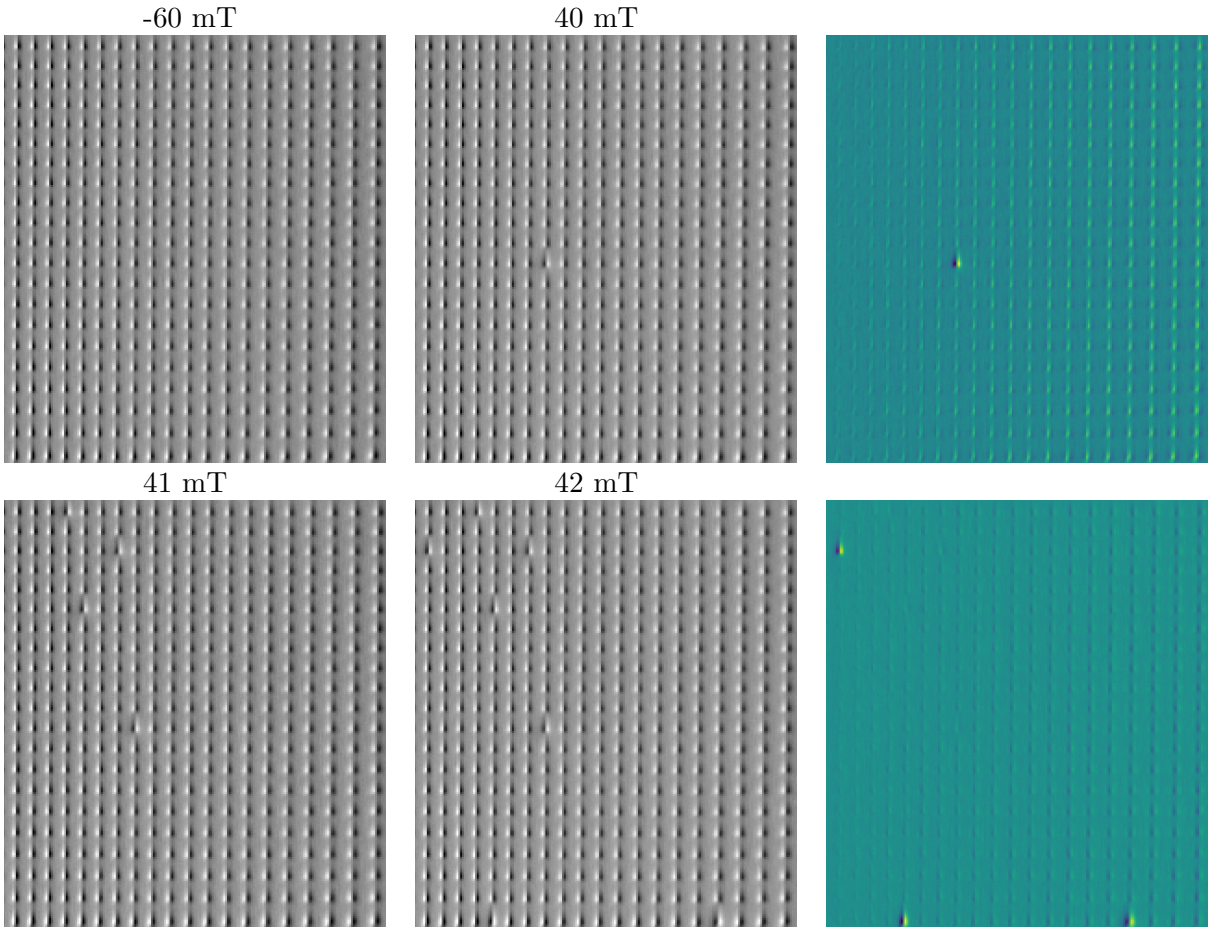

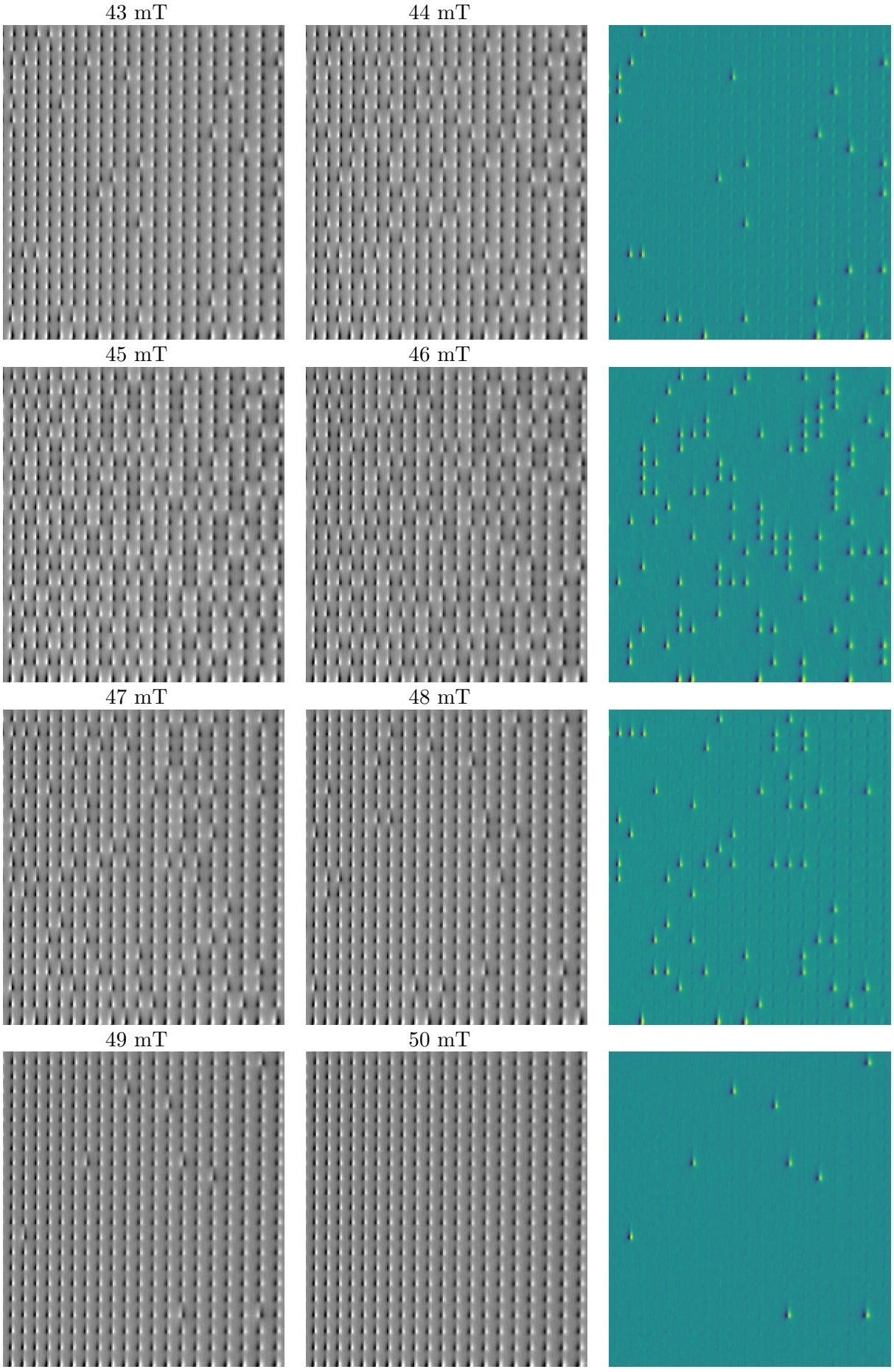
43 mT
44 mT
45 mT
46 mT
47 mT
48 mT
49 mT
50 mT